ISSN 1385-8947

ELSEVIER

CEJ

CHEMICAL ENGINEERING JOURNAL

Actions for selected articles

Select all / Deselect all

Download PDFs

Export citations

Show all article previews

Contents

Review

Environmental Chemical Engineering

Chemical Reaction Engineering

Novel Materials for Energy and Advanced Applications

Research article ● Full text access

Injectable photocrosslinkable acellular cartilage matrix hydrogel loaded with exosomes for promoting growth plate injury repair

Xinxin Si, Quan Zhang, Bo Ning, Lei Qiang, ... Pengfei Zheng

Article 152463

View PDF Article preview

Research article ● Full text access

Endowing calcium phosphate ceramics with long-acting antibacterial capacity by constructing multilevel antibiotic release structure for regenerative repair of infected bone defect

Cong Feng, Qingqing Ren, Tinghan He, Puxin Liu, ... Xiangfeng Li

Article 152255

View PDF Article preview

Research article ● Full text access

Dynamic processes of positive/negative immune-vascular crosstalk loop *via* functional MRI-guided monitor

Chemical Engineering Journal 493 (2024) 152463

Contents lists available at ScienceDirect

Chemical Engineering Journal

journal homepage: www.elsevier.com/locate/cej

Injectable photocrosslinkable acellular cartilage matrix hydrogel loaded with exosomes for promoting growth plate injury repair

Xinxin Si [a,b,1], Quan Zhang [a,b,1], Bo Ning [c,1], Lei Qiang [a,1], Qiang Li [a], Yihao Liu [a,d], Minjie Fan [a], Jing Shan [e], Guanlu Shen [a,b], Zichen Lin [c], Pengfei Zheng [a,*]

[a] Department of Orthopaedic Surgery, Children's Hospital of Nanjing Medical University, Nanjing, Jiangsu, China
[b] Jiangsu Key Laboratory of Marine Bioresources and Environment, Co-Innovation Center of Jiangsu Marine Bio-industry Technology, Jiangsu Key Laboratory of Marine Pharmaceutical Compound Screening, Jiangsu Ocean University, Lianyungang, China
[c] Department of Pediatric Orthopaedics National Children's Medical Center, Children's Hospital of Fudan University, Shanghai, China
[d] Shanghai Key Laboratory of Orthopaedic Implant, Department of Orthopaedic Surgery, Shanghai Ninth People's Hospital, Shanghai Jiao Tong University School of Medicine, Shanghai, China
[e] School of Pharmacy, The University of Sydney, Sydney, NSW 2006, Australia

ARTICLE INFO

Keywords:
Exosomes
Acellular cartilage matrix
Chondrogenic differentiation
Growth plate injury
Tissue engineering

ABSTRACT

The growth plate is vital for childhood development, and most of the injuries can formation of bone bridges on it, which has negative impact on limb development. Current biomaterial scaffolds often lack essential cartilage matrix components, which hurdles to get an acceptable regeneration. Additionally, stem cell transplantation faces challenges including high apoptosis rates and uncertain differentiation. Then, we designed an injectable composite hydrogel (Exo-AMG) loaded with exosomes (Exo) and composed of methacrylate-modified acellular cartilage matrix (ACMMA) and gelatin methacrylate (GelMA) to repair the growth plate for children and adolescents. The hydrogel is administered via minimally invasive injection and undergoes *in-situ* photocrosslinking to fill the growth plate defects. It exhibited suitable mechanical properties, biodegradation rates; it also could sustain exosome release. Moreover, it promoted M2 macrophage polarization and secretion of anti-inflammatory factors, and it enhanced bone mesenchymal stem cells (BMSCs) proliferation and chondrogenic differentiation *in vitro*. *In vivo* study, this Exo-AMG induced growth plate cartilage regeneration without bone bridge formation. Therefore, this injectable and *in-situ* photocrosslinkable composite hydrogel is promising on growth plate injury repair by alleviating inflammation and promoting chondrogenic differentiation.

1. Introduction

The growth plate, positioned between the epiphysis and metaphysis of long bones, is integral to the longitudinal growth of tubular bones during childhood [1]. The growth plate tissue, which is the most vulnerable section of long tubular bones, is susceptible to injuries arising from diverse factors [2]. Due to its limited self-repair capabilities, the growth plate is prone to the development of bony connections between the epiphysis and metaphysis after injury, commonly known as a bone bridge [3]. The shortening and angular deformities, resulting from bone bridge varies depending on its location and extent, significantly hurdles the normal growth of the affected limb [4]. Current clinical treatments, including bone bridge excision and the use of polymeric materials, are unsatisfactory to prevent bone bridge regeneration [5]. However, due to lacking the ability to promote growth and reconstruct growth plate tissue, these materials are limited effectiveness on small-area (<30 %) growth plate injuries [6]. Researchers endeavor to develop biologically active materials capable of filling growth plate defects, preventing bone bridge recurrence, and restoring the surrounding undamaged growth plate tissue's ability for longitudinal bone growth [7]. Tissue engineering is an effective strategy for regenerating growth plate cartilage and promoting functional recovery after injury, with key components including seed cells, bioactive factors, and scaffold materials [8].

Adequate seed cells serve as the fundamental basis for tissue regeneration. BMSCs are highly sought-after for transplantation due to their validated efficacy in preventing bone bridge formation, enhancing

* Corresponding author.
E-mail address: zhengpengfei@njmu.edu.cn (P. Zheng).
[1] The first four authors contributed equally to this work.

https://doi.org/10.1016/j.cej.2024.152463
Received 16 March 2024; Received in revised form 9 May 2024; Accepted 20 May 2024
Available online 22 May 2024

growth plate repair, and correcting limb length discrepancies [9]. Nevertheless, the pathological microenvironment following growth plate injury can lead to poor survival rates and non-therapeutic differentiation of implanted BMSCs [10,11]. Recent studies indicate that BMSCs may regulate the damaged tissue microenvironment through the paracrine effects of exosomes, mediating cartilage tissue repair and regeneration [12–14]. Exosomes play a pivotal role as essential carriers for intercellular endocytosis to influence various biological processes such as cell proliferation, differentiation, tumor immunity, and inflammatory responses [15–17]. Derived from BMSCs, the exosomes are lipid membranes which envelope microRNAs, mRNAs, and proteins, to facilitate their delivery to receptor cells [18]. The exosome function is through diverse signal transduction pathways [19,20]. Although it is similar to BMSCs, the exosomes possess stable properties with lower storage and transportation demands, reducing the risks associated with direct stem cell transplantation [21]. Consequently, these exosomes are deemed an ideal alternative to BMSCs in "cell-free" tissue engineering strategies.

Scaffold materials serve as temporary substitutes for the natural extracellular matrix (ECM), providing a microenvironment for cell survival and facilitating the rebuilding of the basic framework of growth plate. Extracellular matrix scaffolds have gained widespread use in tissue engineering due to its excellent biocompatibility and bioactivity [22–24]. Acellular cartilage matrix (ACM) removes immunogenic cells while it retains bioactive factors and natural extracellular matrix [25]. It can offer a chondrogenic microenvironment, similar to native tissue [26]. Therefore, it supports cell adhesion, growth and differentiation. However, some studies show that scaffolds only can temporarily delay bone bridge formation due to ACM rapid degradation [27,28]. Moreover, the deformities will occur after the scaffold absorption [29].

To address these challenges, methacrylate-modified acellular cartilage matrix (ACMMA) is prepared in this study through physical crushing, enzymatic hydrolysis, and chemical modification. Compared to ACM, ACMMA has photocrosslinking capabilities, significantly enhancing its constructability and physical properties. Nevertheless, its structural stability and shape retention still cannot fully match the growth plate cartilage regeneration microenvironment requirements [28]. To compensate these, we propose the combining ACMMA with other polymeric materials. Gelatin methacryloyl (GelMA) holds promise in cartilage defect repair materials due to its controllable degradation, mechanical properties, and excellent biocompatibility [30]. Therefore, the combining ACMMA with GelMA is suitable for an injectable, in-situ

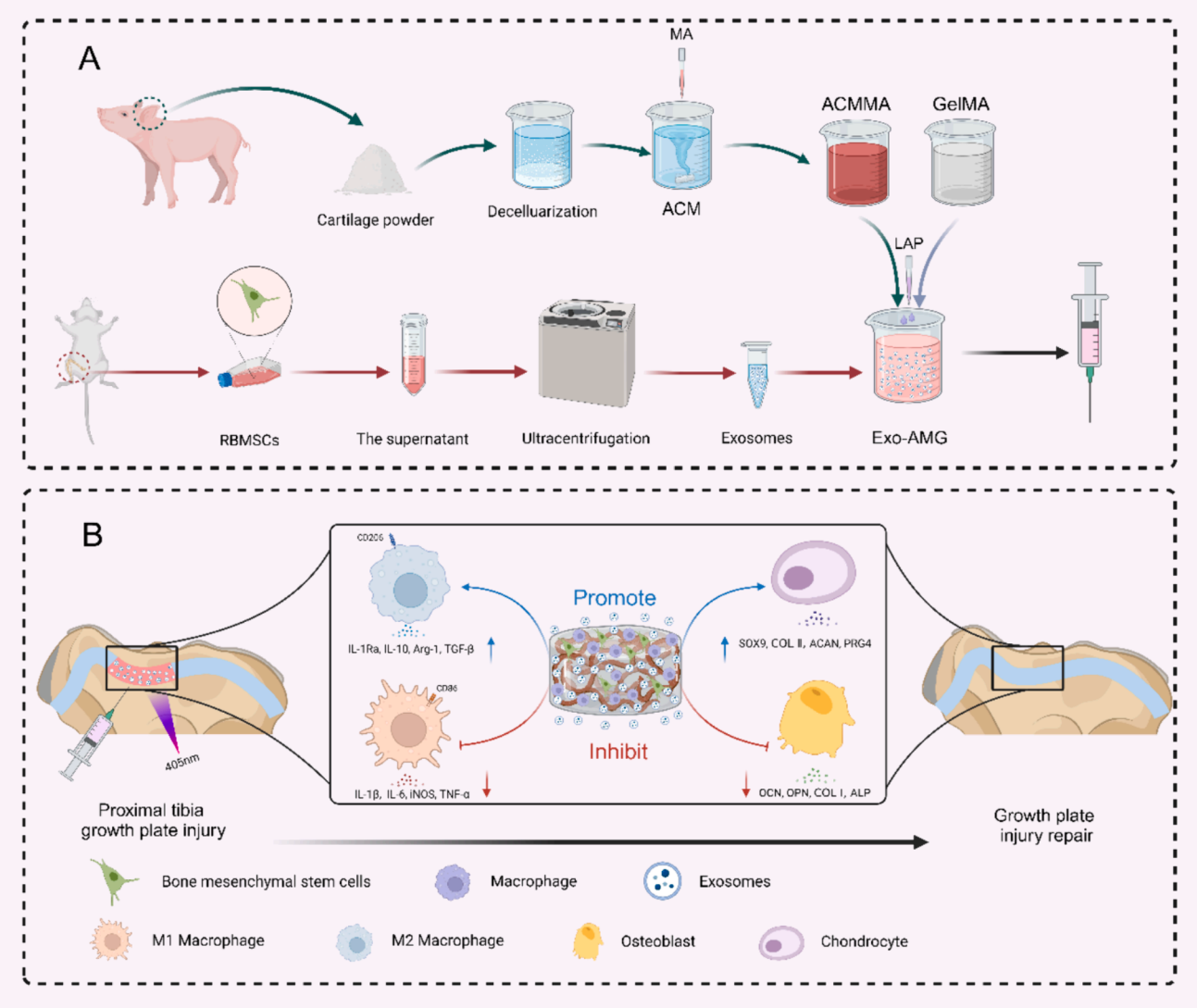

Scheme 1. The combination of novel photocrosslinked hydrogels with RBMSCs-derived exosomes exhibits significant advantages in repairing the growth plate. (A) Procedures for preparation of composite hydrogels. (B) The novel photo-crosslinked hydrogel exhibits instant *in-situ* seamless adhesiveness, effectively filling the growth plate injury site. It preserves the functionality of RBMSCs-derived exosomes, inhibits inflammatory reactions, promotes chondrogenic differentiation, and achieves regeneration of the growth plate cartilage.

photocrosslinked ACMMA-GelMA (AMG) composite hydrogel scaffold, mimicking the natural growth plate extracellular matrix and seamlessly filling growth plate defect sites. Furthermore, the rat bone marrow mesenchymal stem cell-derived exosomes are mixed into AMG to prepare the Exo-loaded AMG hydrogel (Exo-AMG). The feasibility of growth plate regeneration and repairment are explored through *in vitro* and *in vivo* experiments (Scheme 1).

2. Materials and methods

2.1. Materials

GelMA and lithium phenyl-2,4,6- trimethyl benzoyl phosphinate (LAP) were purchased from EFL-Tech Co.,Ltd (Suzhou, China). Fetal bovine serum (FBS), Penicillin-Streptomycin Solution (PS), Minimum Essential Medium α (α-MEM), Dulbecco's modified Eagle's medium (DMEM) and Trypsin were obtained from Gibco (Grand Island, USA). Bicinchoninic acid (BCA) reagent test kit, Cell Counting Kit-8(CCK8) kit, DiI Fluorescent Staining Kit and Calcein-AM/PI staining kit were purchased from Beyotime Biotechnology (Shanghai, China). MolPure® Cell/Tissue Total RNA Kit, Hifair® II 1st Strand cDNA Synthesis SuperMix and Hieff® qPCR SYBR Green Master Mix were purchased from Yeasen Biology (Shanghai, China). The animal surgical procedures involved in this study follow the experiments were reviewed and approved by the Ethics Committee of Children's Hospital of Nanjing Medical University (202202172-1).

2.2. Isolation and culture of rat bone marrow mesenchymal stem cells

Four-week-old Sprague-Dawley (SD) rats were sourced from Shanghai Shengchang Biotechnology Co., Ltd. (China). As described previously, the rat bone marrow mesenchymal stem cells (RBMSCs) were isolated from the femur and tibia [31]. RBMSCs were cultured in α-MEM medium supplemented with 10 % (v/v) FBS and 1 % PS. Cultures were maintained in a 5 % CO_2 incubator at 37 °C, with the culture medium refreshed every 3 days. Passaging was carried out upon reaching 90 % confluence, and cells from passages 3 to 5 were selected to ensure optimal cell viability for the experiment.

2.3. Extraction and identification of exosomes

Exosomes were isolated and purified from RBMSCs using established protocols as described in previous studies [32]. When cell fusion reached approximately 60 %, the culture medium was substituted with α-MEM medium containing 10 % Exo-free serum. Following 48 h of culture (until cells were approximately 100 % fused), the cell culture supernatant was collected aseptically. Exosomes were extracted through a differential ultracentrifugation method, involving sequential centrifugation at 300 × *g*, 2000 × *g*, 10,000 × *g*, and 100,000 × *g*. The resulting pellet was resuspended in a small volume of phosphate-buffered saline (PBS), quantified using the BCA method, and stored at −80 ℃. Exosome morphology was examined by transmission electron microscopy (TEM; Thermofisher, USA) following a published protocol [32]. Particle size analysis of exosomes was conducted using Nanoparticle Tracking Analysis (NTA; Particle Matrix, Germany) at 11 different locations. Additionally, western blotting technique was employed to confirm the presence of CD9, TSG101, and Calnexin in the isolated exosomes.

2.4. Preparation of acellular cartilage matrix and its decellularized efficiency

The ACM was prepared using a modified method as previously described [28]. Pig ears, obtained from a local slaughterhouse, were meticulously skinned, and the remaining ear cartilage tissue was cut into small pieces. These cartilage pieces were then freeze-dried and ground into powder using an automatic sample freeze-grinding machine (Shanghai Jingxin Co., Ltd, China). The cartilage powder underwent treatment with trypsin solution (containing 0.5 wt% trypsin and 0.02 wt % EDTA in PBS) for 24 h, with fresh trypsin replaced every 4 h. Sequential treatments followed with a nuclease solution (containing 50 U/ml deoxyribonuclease and 1 U/ml ribonuclease A in 10 mM Tris-HCl, pH = 7.5) for 4 h, 10 mM Tris-HCl (including 10 KIU/ml aprotinin) for 20 h, and 1 % Triton X-100/PBS solution (v/v) for 24 h. The resulting decellularized cartilage powder was obtained by freeze-dried after being washed six times in PBS. After being freeze-dried, the decellularized cartilage powder (10 mg/ml) underwent enzymatic digestion in a pepsin solution (containing 2 mg/ml pepsin in PBS, pH 2–3) at 37 °C with constant oscillation for 24 h. The viscous solution formed was neutralized to a pH of 7 using 5 M NaOH solution and subjected to dialysis using a 3500D molecular weight cutoff membrane in deionized water for 72 h. The resulting ACM was freeze-dried and stored at −20℃ until use. All reagents were supplied by Sigma-Aldrich.

To evaluate the decellularization efficiency, histological sections were analyzed with H&E and DAPI staining. The residual DNA and ECM components such as collagen and glycosaminoglycans (GAG), were quantitatively assessed. For quantification, the ACM was digested in papain solution (125 μg/mL papain, 0.1 M Na_3PO_4, 5 mM Na_2EDTA, 5 mM cysteine-HCl, pH 6.5) for 12 h at 60 ℃. The digestive fluid was then centrifuged at 10,000g/min for 30 min, and the upper layer solution was collected for quantitative analysis. Native tissues of similar weight were also digested as controls. Quantitative analysis of extracellular matrix (ECM) components, including collagen, GAG, and residual DNA, was performed using a hydroxyproline (HYP) content assay kit (Solarbio, China), GAG quantification assay kit (Genmed, China), and dsDNA HS Quet assay kit (Yeason, China), respectively.

2.5. Methacrylation of acellular cartilage matrix

To formulate a photocrosslinkable hydrogel, ACM was modified by adding methacrylic anhydride (MA; Sigma-Aldrich), following procedures detailed in previous studies [28]. Briefly, 0.5 g of water-soluble ACM was dissolved in deionized water, and 0.5 mL of MA was gradually added at a rate of 0.5 mL/min within an ice bath. The pH was maintained between 8 and 10 using 5 M NaOH, and the reaction proceeded overnight with continuous stirring. After the reaction, the solution was neutralized with 1 M HCl, dialyzed using a 3,500 D membrane in distilled water for one week, and then freeze-dried.

Dissolve the freeze-dried ACM and ACMMA separately at a concentration of 10 mg/mL in deuterated water (D_2O). Record the spectra of the pure ACM and ACMMA using a ^1H Nuclear Magnetic Resonance system (^1H NMR) at room temperature. Fourier transform infrared spectroscopy (FTIR) was used to characterize the chemical properties of ACM and ACMMA in the wavenumber range of 4000–400 cm^{-1}, analyzing functional groups and chemical bonds.

In terms of the synthesis principle of ACMMA, degrees of amino substitution (DAS) are the ratio of amino groups in ACM that are replaced by methacrylate groups during the synthesis of ACMMA [33]. DAS was confirmed using a 2,4,6-trinitrobenzene sulfonic acid (TNBS; Sigma-Aldrich) assay. TNBS reacts with amino groups, exhibiting a characteristic UV absorption peak at 425 nm. Therefore, it can be used for quantitative determination of the number of amino groups in ACM and ACMMA. degrees of amino substitution (DAS) for ACMMA can be measured using the following formula:

$$DAS = \frac{OD_{ACM} - OD_{ACMMA}}{OD_{ACM}} \times 100\%$$

The injectability of composite hydrogels was evaluated by introducing the ACMMA prepolymer solution (10 wt% ACMMA, 0.5 wt% LAP) mixed with red pen ink through a 1 mL syringe (needle diameter = 0.5 mm). The gelation solidification time was determined through the following procedure: The ACMMA prepolymer solution was injected

into the base of a glass vial, and the vial was continuously tilted under ultraviolet (UV) light (405 nm, 283 mW/cm^2). The flow behavior of the prepolymer solution was observed, and the gelation time was recorded when the solution ceased to flow during the tilting process. This marked the formation of the ACMMA hydrogel, and the corresponding gelation time was documented.

2.6. Preparation of composite hydrogels

Different ratios of ACMMA and GelMA were introduced into a photoinitiator solution (containing 0.5 wt% LAP in PBS), and the mixture was dissolved under light-protected conditions with stirring at 37 °C. The compositions and abbreviations of the hydrogels used in this study are presented in Table 1. After thorough stirring, the pre-polymer solution of each group was added to the polytetrafluoroethylene molds. Subsequently, the mixture underwent photopolymerization under UV light at a wavelength of 405 nm for 30 s. Upon solidification, the hydrogels were demolded and stored for subsequent use.

2.7. Characterization of composite hydrogel

The hydrogel scaffolds, prepared as outlined previously, underwent cryogenic fracturing using liquid nitrogen following freeze-dried. Scanning electron microscopy (SEM; TESCAN, Czech) with a 5 kV accelerating voltage was employed to examine the morphological characteristics of cross-sectional images obtained from the freeze-dried hydrogels.

For the determination of scaffold porosity, a liquid displacement method was utilized. Anhydrous ethanol, chosen for its non-swelling or shrinkage effect on the hydrogel, served as the liquid for porosity measurement. The known dry weight of the scaffold was immersed in anhydrous ethanol. The freeze-dried hydrogel, saturated with anhydrous ethanol, was placed in a glass bottle containing anhydrous ethanol with a volume of V_1. After 48 h of soaking, the total volume of anhydrous ethanol and the freeze-dried scaffold were denoted as V_2. The remaining volume of anhydrous ethanol after the gradual removal of the scaffold was recorded as V_3. The porosity of the hydrogel scaffold was then calculated using the following formula:

$$Porosity = \frac{V_1 - V_3}{V_1 - V_2} \times 100\%$$

The mechanical properties of each group's hydrogels were assessed using a mechanical testing machine (Hengyi, China). Uniaxial compression testing was performed on each composite hydrogel sample at a constant strain rate of 1 mm/min and a temperature of 25 ℃. The test frequency ranged from 0.1 to 5 Hz, and the elastic modulus was calculated by determining the slope of the stress–strain curve within the 0 %–40 % strain range.

For each group of composite hydrogel samples, the initial freeze-dried weight was denoted as M_0. Each 10 mg freeze-dried hydrogel scaffold was placed in 1 mL of PBS at 37 °C. To assess *in vitro* degradation performance, hydrogel scaffolds from each group were retrieved and freeze-dried at five time points (3, 7, 14, 21, 28 days), with the resulting weights recorded as Mt. The degradation rate of the hydrogel scaffold was calculated using the following formula:

$$Degradation = \frac{M_0 - M_t}{M_0} \times 100\%$$

After freeze-dried, the dry weight (M_d) of each hydrogel sample was recorded. Subsequently, the samples were immersed in a PBS solution and allowed to swell to equilibrium at a constant temperature of 37 °C for 24 h. The swollen hydrogel samples were then extracted, excess surface water was removed with filter paper, and the swollen mass (M_w) was recorded. The swelling ratio of the hydrogel samples was calculated based on the weight change. Each group was measured in triplicate, and the swelling ratio was determined using the following formula:

$$Swellingratio = \frac{M_w}{M_d}$$

Rheological measurements were performed using a Haake Mars Modular Advanced Rheometer (Thermo Fisher Scientific, USA). The kinetic viscosity experiment (0.1–100 s^{-1}) with constant strain was conducted at room temperature to evaluate the viscosity properties of various hydrogels. A frequency sweep test, conducted at a fixed strain of 1 % and ranging from 0.1 to 100 rad s^{-1}, was employed to obtain the storage modulus (G′) and loss modulus (G″).

2.8. Exos release profile

Cumulative release profiles were assessed utilizing a bicinchoninic acid (BCA) reagent test kit. Exosomes labeled with DiI red fluorescent dye (500 μg) were combined with 200 μL of AMG pre-polymer solution, and the mixture underwent photocrosslinking under UV light (405 nm, 283 mW/cm^2). Confocal laser scanning microscopy (Leica, Germany) was employed to observe the spatial distribution of DiI-labeled exosomes. To assess the *in vitro* release performance of exosomes, the Exo-AMG hydrogel was immersed in 2 mL PBS at 37 °C, and supernatant was collected on days 1, 3, 5, 7, 9, 11, 13, 15, 17, 19, and 21. Fresh PBS was added after each collection. The concentration of free exosomes in the supernatant was determined using the BCA reagent test kit, and release curves along with cumulative release curves were recorded and plotted.

2.9. In vitro biocompatibility assessment

In vitro biocompatibility assessments were performed by incorporating cell viability, proliferation, and adhesion experiments. For the Live/Dead staining experiment, 1 × 10^5 RBMSCs were seeded into hydrogel discs and co-incubated with each sample for 72 h. Similarly, RAW 264.7 cells were seeded into hydrogel discs at the same cell density and co-cultured with each sample for 72 h. Subsequently, a Live/Dead staining solution (Yeasen, China) was prepared in a ratio of 1 mL: 3 μL: 5 μL (PBS: calcein-AM: PI) and added to each group, followed by incubation at 37 °C for 30 min. Fluorescent images of live/dead cells were captured using a confocal laser scanning microscope. For the longitudinal growth experiment, 2 × 10^5 RBMSCs were seeded into Exo-AMG hydrogel discs. After co-culturing for 7 days, staining solution (containing 3 μL calcein-AM in 1 mL PBS) was added, followed by incubation at 37 °C for 30 min. The cell growth was observed using a confocal laser scanning microscope. Moreover, RBMSCs and RAW 264.7 were seeded on hydrogel discs for each group (1 × 10^5 cells/well) to monitor the cell proliferation on hydrogels. At the designed time points, each set of samples underwent co-incubation with culture medium containing 10 % CCK-8 reagent, maintained in the dark at 37 °C for 1 h. Following the incubation, the absorbance of the supernatant was measured at 450 nm wavelength using a microplate reader.

Table 1
The composition of different composite hydrogel.

Samples	Composition (% w/v)		
	ACMMA	GelMA	LAP
ACMMA	10 %	0 %	0.5 %
A9G1	9 %	1 %	0.5 %
A7G3	7 %	3 %	0.5 %
A5G5	5 %	5 %	0.5 %
A3G7	3 %	7 %	0.5 %
A1G9	1 %	9 %	0.5 %
GelMA	0 %	10 %	0.5 %

2.10. Internalization assay in vitro

DiI-labeled exosomes were amalgamated with the AMG pre-polymer solution, resulting in the formation of a hydrogel through photo-crosslinking. The exosome-loaded composite hydrogel scaffold was then immersed in 2 mL α-MEM complete culture medium and extracted for 24 h at 37 °C in the absence of light. The resulting extraction solution was collected and co-cultured with RBMSCs for 12 h. Following this, cells were PBS-washed, fixed with 4 % paraformaldehyde for 15 min, and stained with FITC (Kingmorn, China) for the cell cytoskeleton over 15 min, followed by DAPI (Aladdin, China) staining for cell nuclei for 5 min. Ultimately, the cellular uptake of exosomes was observed utilizing confocal laser scanning microscopy.

2.11. Transwell migration assay

Following the photocrosslinking of 200 μL of each hydrogel pre-polymer solution in the mold, the hydrogel samples were immersed in 2 mL of α-MEM complete culture medium and extracted at a constant temperature of 37 °C for 24 h. The extraction solutions from each group of the composite hydrogel scaffolds were collected. RBMSCs were resuspended in α-MEM culture medium containing 5 % FBS to a concentration of approximately 1×10^5 cells/ml. Next, 500 μL of each group's extraction solution was added to the bottom layer of a Transwell plate, and 200 μL of the cell suspension was slowly transferred to the upper chamber of the Transwell plate. The Transwell chambers, along with the cells, were cultured at 37 °C with 5 % CO_2 for 12 h. After 12 h, the Transwell chambers were removed, and the culture medium in the upper chamber was carefully aspirated. The cells in the upper chamber were gently wiped off with a moist cotton ball, and the chamber was fixed in 4 % paraformaldehyde for 15 min. The fixed cells were stained with 0.1 % crystal violet dye (Beyotime, China) in the dark for 20 min. After washing three times with distilled water, cell migration was observed under an inverted light microscope (Olympus, Japan).

2.12. Toluidine blue staining

To assess the chondrogenic differentiation potential of each hydrogel scaffold, an *in vitro* staining of the chondrocyte-specific extracellular matrix was conducted using Toluidine blue. The hydrogel precursor solution (200 μL) was cross-linked and incubated in 2 mL chondrogenic induction medium (containing 100 nM dexamethasone, 25 mg/ml vitamin C, 40 mg/ml proline, 10 ng/mL TGF-β3, and 1 % ITS-G in α-MEM medium) at 37 °C for 24 h. The resulting extraction from each composite hydrogel scaffold was collected. RBMSCs (1×10^4 cells/well) were seeded in a 12-well plate, and upon complete cell adhesion, the α-MEM culture medium was replaced with chondrogenic induction extraction. After 3 weeks of chondrogenic induction, an Alcian Blue staining experiment was performed. The culture dish containing RBMSCs was fixed with 4 % paraformaldehyde (Biosharp, China) for 30 min at room temperature, followed by three washes with deionized water. Toluidine blue staining was conducted using the Toluidine Blue staining kit (Sangon, China) according to the manufacturer's instructions for 15 min. Subsequently, the samples were washed three times with deionized water, and the staining results were observed under an inverted light microscope.

2.13. Gene expression analysis

Total cellular RNA extraction was carried out using the MolPure® Cell/Tissue Total RNA Kit, followed by reverse transcription into cDNA using the Hifair® II 1st Strand cDNA Synthesis SuperMix. For RT-PCR analysis, the Hieff® qPCR SYBR Green Master Mix was utilized. The relative gene expression was quantified using the $2^{-\Delta\Delta Ct}$ method. Three independent experiments were conducted, and the primer sequences used in this study are outlined in Table S1.

2.14. Western Blot

Cell homogenization was conducted in RIPA buffer containing protease and phosphatase inhibitors, and supernatants were obtained by centrifugation at 12,000 rpm at 4 °C for 30 min after lysing on ice for 30 min. The total protein concentration was determined using the BCA kit (Beyotime, China). The supernatants were combined with loading buffer (Beyotime, China), and equal amounts (40 μg) of protein were loaded onto sodium dodecyl sulfate–polyacrylamide gel electrophoresis (SDS-PAGE).

Following protein separation, the proteins were transferred to a polyvinylidene difluoride (PVDF, Thermo Fisher) membrane. The PVDF membrane was blocked with 5 % skim milk for 1 h and then incubated overnight with the primary antibodies (refer to Table S2). Subsequently, the PVDF membrane underwent a 1-hour incubation with the secondary antibody before visualization with the enhanced chemiluminescence (ECL) kit (Biomart, China). Tris Buffered Saline with Tween® 20 (Epizyme, China) was employed for thrice membrane washes before each step. The results were analyzed using Image J software.

2.15. In vivo growth plate regeneration

Animal experiments were conducted following approval from the Ethics Committee of Nanjing Medical University, adhering strictly to the guidelines outlined in the National Institutes of Health for the care and use of laboratory animals. Twenty-four male New Zealand white rabbits, 6 weeks old, were obtained from Nanjing Medical University and randomly assigned to four groups: Control, GelMA, AMG, Exo-AMG.

To assess the hydrogels' efficacy in repairing growth plate injuries, we employed a proximal tibial growth plate injury model, as described in previous studies [34]. Following anesthesia administration, the surgical site, extending from the medial malleolus to the pelvis, was depilated and sterilized. A 2 cm skin incision was made from the medial knee joint towards the proximal tibia. The proximal tibial growth plate was exposed to soft tissue dissection, and a precise 0.5 cm incision was made from the growth plate to the lower end of the skin incision. Using a 3 mm-diameter drill at 10,000 rpm, a cortical window was created in the tibial stem, and the drill penetrated the growth plate. Hydrogel from each group was injected into the defect, crosslinked under 405 nm ultraviolet light for 30 s, and solidified. The surgical site was then sutured layer by layer.

Post-surgery, rabbits were housed separately without limb immobilization, and intramuscular penicillin injections (20,000 units/kg) were administered for infection prevention for 3 days. One month after surgery, half of the rabbits in each group were euthanized, with the remaining rabbits euthanized after 3 months. Growth plate cartilage repair and regeneration was evaluated in histological sections of the lower limb through the use of H&E, Toluidine blue (TB), and Alcian blue (AB) staining.

2.16. Statistical analysis

Statistical analysis was performed using GraphPad Prism 5 software and SPSS version v19.0.0 (IBM, USA). Nonparametric Kruskal-Wallis test or one-way analysis of variance (ANOVA) with Tukey's test was employed. The experimental results were presented as mean ± standard deviation (Mean ± SD). Each experiment was conducted independently at least three times to ensure reliability. $P < 0.05$ was the threshold of significance.

3. Results and discussion

3.1. Characterization of RBMSCs-Exos

The RBMSCs-conditioned medium, cultured in serum-free exosome medium, was collected. Differential ultracentrifugation was employed

to isolate and enrich RBMSCs-derived exosomes by stepwise removal of impurities at different speeds and durations (Fig. 1A). The extracellular vesicles were observed by transmission electron microscopy, exhibited a typical discoid shape with a diameter of approximately 100 nm and intact double-membrane structures (Fig. 1B), consistent with the characteristic morphology of exosomes [20]. Nanoparticle tracking analysis (NTA) of the isolated extracellular vesicles revealed a predominant size distribution between 100–200 nm, with a peak diameter of 165 nm, which aligns with the standard size range for exosomes (Fig. 1C). Western blotting results demonstrated high expression of exosomal protein markers CD9 and TSG101 in the isolated extracellular vesicles, while the intracellular protein Calnexin was not expressed (Fig. 1D). These findings confirm that the extracted samples indeed represent exosomes.

3.2. Characterization of photocrosslinkable acellular cartilage matrix hydrogels

The decellularization process for cartilage tissue is intricate, given its avascular nature and dense ECM structure [35]. An effective decellularization method should remove cellular components but preserving other constituents, such as collagen, glycosaminoglycans and growth factors, to maintain the structure and biomechanical properties of the ECM. This research utilized a combination of physical treatments, chemical agents, and biological nucleases for decellularization (Fig. 2A). This approach not only successfully removed cellular components and reduced immunogenicity, but also enhanced the penetration of chondrocytes and stem cells, which could facilitate natural infiltration and repopulation of the cartilage scaffold and promote cartilage regeneration [36].

After decellularization, the cartilage slices maintained a similar appearance to untreated cartilage. The results of magnified H&E and DAPI (blue) staining images showed that the primary ECM was well-preserved, with minimal visible cell nuclei (Fig. 2B). Biochemical analysis of the cartilage before and after decellularization (Fig. 2C–E) indicated that collagen and GAG were largely retained in the ACM while DNA was effectively removed, which was consistent with the histological observations in Fig. 2B. Some studies has demonstrated that the decellularized ECM with a lower DNA content (less than 50 ng/mg or 3 w/v% of DNA) does not induce immune rejection when implanted into a different species [37]. Therefore, the key aspect of decellularization is to eliminate residual DNA content. Moreover, the DNA content in the ACM was approximately 19.8 ± 5.45 ng/mg, below the immune rejection threshold when different cells grow on ECM. Hence, all results affirm the success of the decellularization process, and the ACM can be used for further construction of tissue engineering scaffolds.

Despite some significant progress, current acellular cartilage matrix (ACM) biomaterials still exhibit their limitations in constructive and mechanical stability, which can impact practical applications [38]. In response to this challenge, we introduced MA for ACM modification, which resulted in the creation of ACMMA with rapid photocrosslinking characteristics. The structural features of ACMMA and photocrosslinking mechanism, transitioned from the flowable pre-polymer solution to the solidified hydrogel under 405 nm UV light, are depicted in Fig. 3A.

We performed ^{1}H NMR and FTIR tests on ACMMA. The signals of methacrylamide groups at 5.4 and 5.6 ppm increased after introducing MA into ACM [28], indicating successful modification of ACMMA (Fig. 3B). The amide A and B bands of ACM shifted to 3318 cm^{-1} and 3075 cm^{-1}, respectively, after methacrylation, mainly representing the stretching vibrations of N-H bonds. The peak at 1654 cm^{-1} was associated with the vibration of the conjugated amide group's C═O, and the peak at 1542 cm^{-1} corresponded to the coupling of N-H bending vibrations and C-N stretching vibrations, indicating the formation of amide bonds [39]. The C-O-C stretching peak of the methacrylic acid group appeared at 1029 cm^{-1} (Fig. 3C). According to the synthesis principle of ACMMA, degrees of amino substitution (DAS) refer to the proportion of amino groups in ACM replaced by methacrylate esters during the GelMA synthesis. The TNBS assay analysis revealed a DAS of 60.22 ± 1.14 % for ACMMA, meeting the requirements for cellular

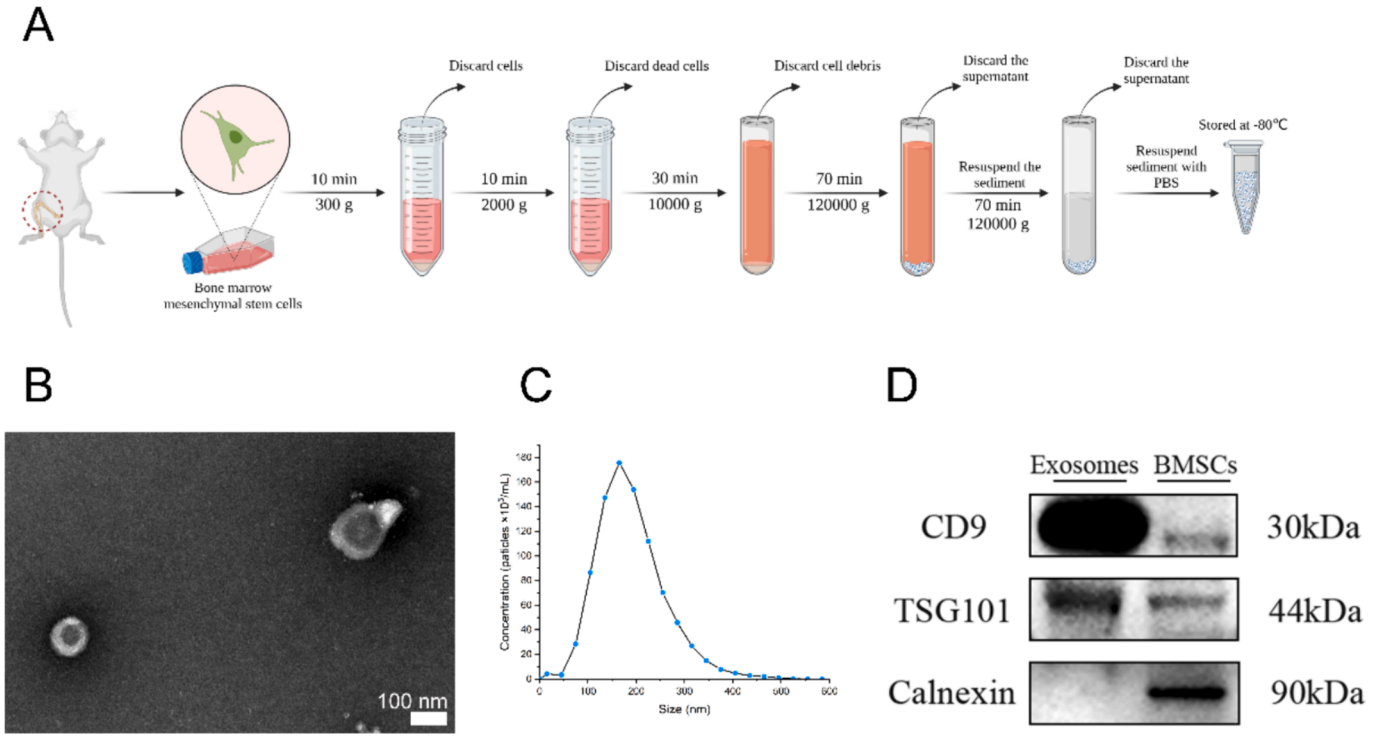

Fig. 1. The extraction and identification of RBMSCs-derived exosomes. (A) Exosomes were isolated through differential ultracentrifugation. (B) Microscopic visualization of the obtained nanoparticles using TEM. (C) Particle size analysis of the nanoparticles conducted through NTA. (D) Evaluation of RBMSCs-Exo markers, including CD9, TSG101, and Calnexin.

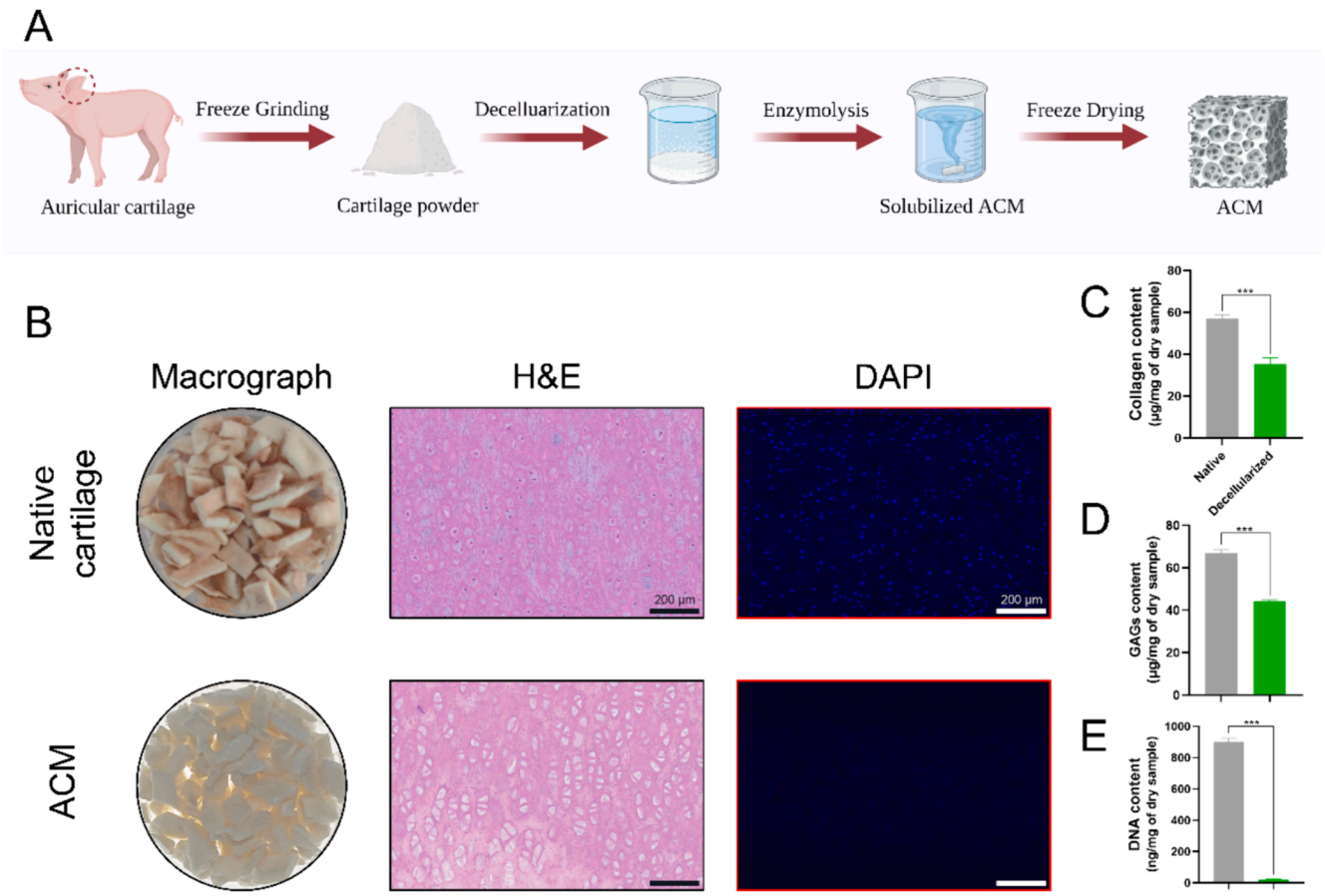

Fig. 2. The preparation and proteomic analysis of acellular cartilage matrix. (A) ACM was prepared utilizing decellularization and enzymolysis procedures. (B) Qualitative assessment of ACM using H&E and DAPI staining methods. (C), (D) and (E) Quantitative analysis of collagen content, GAG content, and DNA content. Data expressed as mean ± SD (n = 3). ***p < 0.001.

loading and culture (DAS < 90 %) [33]. The excellent injectability of the ACMMA hydrogel pre-polymer solution is demonstrated in Fig. S1. After exposure to UV light for 30 s, the hydrogel crosslinked and solidified, transforming from a semi-transparent liquid into an opaque cylinder, as observed in the inclined glass bottle test (Fig. 3C).

The aforementioned results show the presence of methacrylate ester groups on the ACMMA molecules, which confers upon them the potential for polymerization under suitable conditions. In the photocuring process, LAP is typically introduced as the photoinitiator. Photoinitiators generate free radicals under UV light, which attack the double bonds of the methacrylate ester groups to initiate a chain polymerization reaction among the methacrylate ester groups. This leads to the formation of covalent bonds between ACMMA molecules, ultimately constructing a stable three-dimensional crosslinked network structure, which imparts the hydrogel with specific physical strength and stability [28]. The ACMMA pre-polymer solution can be injected into defect sites with complex geometries using a syringe and rapidly crosslinked under UV light, effectively filling the defect.

3.3. Characterization of different ACMMA/GelMA composite hydrogels scaffolds

Compared with ACM, ACMMA has enhanced constructability and physical properties. However, its structural stability and shape retention are limited, precluding its use as a standalone material for cartilage tissue engineering. To address this concern, GelMA was used as an auxiliary material to improve the injectability and stability of the pre-gel solution and to replenish some of the collagen components lost during the decellularization process [28].

In Fig. 4A, the optical images depict the composite hydrogel scaffolds for each group, exhibiting a progressively deepening transition in color from transparent to milky white with increasing ACMMA content. Subsequent freeze-dried and cryofracture in liquid nitrogen enabled the acquisition of scanning electron microscopy (SEM) images showed the cross-sections of the hydrogel scaffolds (Fig. 4B). SEM images revealed a sponge-like porous structure in the cross-sections of the hydrogel scaffolds across all groups. The increased ACMMA content corresponded to a higher degree of scaffold porosity. The quantitative analysis of pore size and pore area supported this observation, indicating an average pore size of approximately 171 ± 3.44 μm and a pore area ratio of about 76.01 ± 1.38 % for ACMMA scaffolds, while GelMA scaffolds exhibited an average pore size of approximately 89.05 ± 1.58 μm and a pore area ratio of around 59.5 ± 0.27 % (Fig. S2 A and B). Porosity measurements using the buoyancy method further affirmed the gradual increase in porosity with an escalating ACMMA content (Fig. 4C). The interconnected porous structure of these hydrogel scaffolds facilitates cell adhesion, migration, and growth, fostering nutrient and waste exchange and contributing to the regenerative microenvironment for growth plate cartilage tissue repair [34]. Due to their hydrophilicity, these hydrogels tend to absorb and retain moisture within their crosslinked polymer networks. Hydrogels with robust swelling properties also support the exchange of internal cell nutrients and metabolic waste. After 24 h of soaking in PBS, the weight of GelMA hydrogel can reach 5.37 ± 0.13 times of its initial dry weight. As ACMMA content increasing, its swelling ratio gradually rose, reaching 8.07 ± 0.25 times when the ACMMA content at 9 wt% (Fig. 4D).

The stress–strain curve results of the hydrogel scaffolds (Fig. 4E) were an inverse correlation between the mechanical properties of the

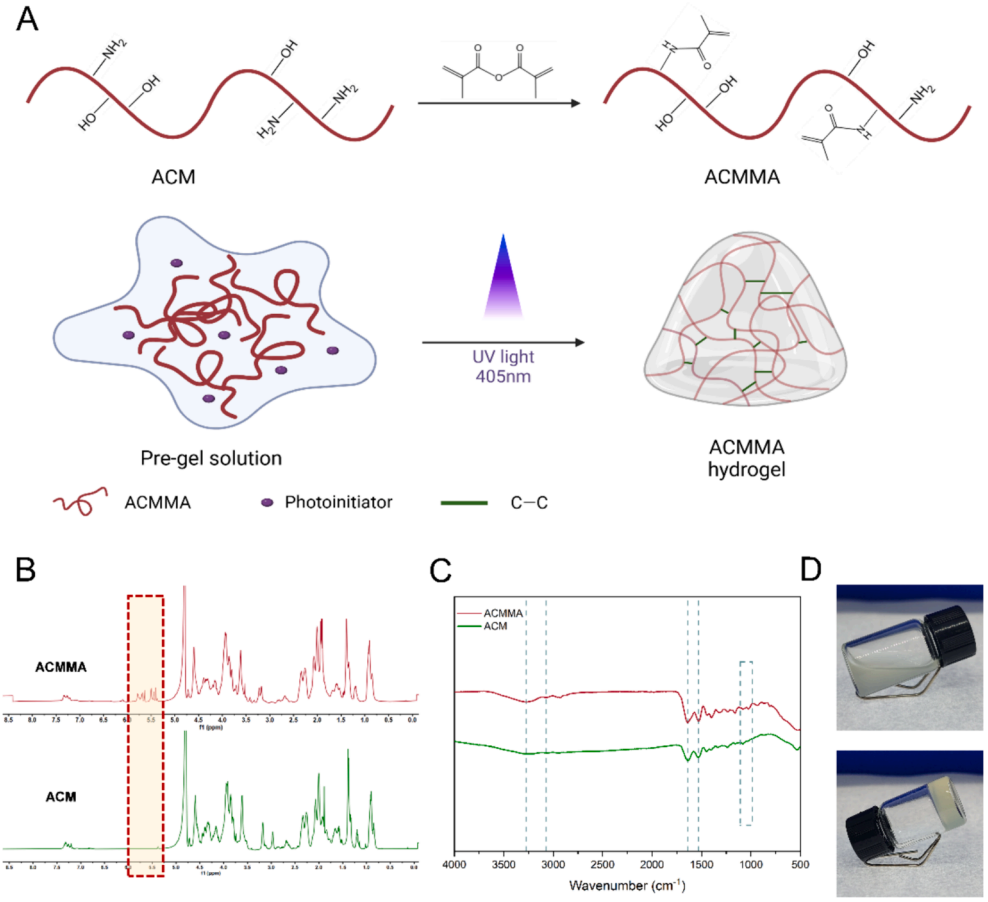

Fig. 3. Physicochemical properties of ACMMA photocrosslinkable hydrogel. (A) Schematic representation of the methacrylate mechanism of ACMMA and the photocrosslinking process, transitioning from the flowable pre-gel solution to cured hydrogels under UV light irradiation (405 nm, 283 mW/cm^2). (B) ^{1}H NMR spectra of ACM and ACMMA. (C) FTIR spectra of ACM and ACMMA. (D) Visualization of the transformation of the flowable ACMMA pre-gel solution into a solid hydrogel through photocrosslinking.

scaffolds and porosity and swelling ratio. The elastic modulus, calculated based on the slope of the stress–strain curve in the 0–40 % strain range, was notably low for ACMMA hydrogel scaffolds, measuring only 5.85 ± 0.21 kPa. With an increasing GelMA content in the composite hydrogel, the elastic modulus gradually rose to 22.27 ± 1.59 kPa (Fig. 4F). Moreover, the degradation rate of the scaffolds increased with the increasement of ACMMA proportion (Fig. 4G). ACMMA, A9G1, and A7G3 fully degraded within 21 days, while the addition of GelMA slowed down the degradation rate of the composite hydrogel scaffolds. A5G5 lost only about 63.42 ± 4.97 % of its dry weight by day 28.

This phenomenon may be attributed to the differing crosslinking densities of ACMMA and GelMA. The ^{1}H NMR spectra (Fig. S3 A) revealed the disappearance of the methyl acrylate peak post photocrosslinking, indicating complete crosslinking of ACMMA. The TNBS assay results showed Gelatin with higher absorbance at 425 nm compared to ACMMA, which indicated the amino groups in ACMMA and Gelatin. These proved a higher amino group content in Gelatin (Fig. S3 B). Moreover, no statistical difference in amino substitution degrees between ACMMA and GelMA was observed (Fig. S3 C). These findings imply that Gelatin offers more amino side chains for methacrylic anhydride modification to yield more methacrylate groups. Via photocrosslinking, GelMA could facilitate more reactions between methacrylate groups, resulting in higher crosslinking density and enhancing hydrogel physical strength and stability. Consequently, with increased ACMMA proportion in the composite hydrogel, hydrogel stability is diminished, and the three-dimensional crosslinking network structure becomes more vulnerable to disruption. *In vitro* degradation rates are escalated, and mechanical properties are weakened.

The rheological results (0.1–100 s^{-1}) (Fig. 4H) demonstrated that the increase in proportion of ACMMA in the pre-gel solution could reduce the viscosity of the solution at room temperature. Regardless of the angular frequency, the hydrogels in each group exhibited relatively stable storage modulus (G') and loss modulus (G''). Both G' and G'' curves did not converge, with G' significantly greater than G'', indicating that the hydrogels in each group are internally stable viscoelastic solids (Fig. 4I and J).

These findings illustrate that all the composite hydrogels possess high water content and a porous structure, conducive to the growth of stem cells. Previous research has indicated that stem cells can perceive the mechanical properties of the extracellular matrix and, to some extent, regulate the differentiation tendency of cells [40]. In a microenvironment with an elastic modulus of 2.5–5 kPa, stem cells favor differentiation into adipocytes, whereas in environments with an elastic modulus of around 13 kPa, stem cells tend to differentiate into chondrocytes [41]. The A5G5 group exhibited an elastic modulus of 13.73 ± 1.2 kPa. Considering the impact of the ACMMA and GelMA ratio on the multifunctional properties of composite hydrogels, the A5G5 group's elastic modulus and degradation rate are suitable for cartilage regeneration. Therefore, in all subsequent experimental studies, we adopted the A5G5 group, named ACMMA/GelMA composite hydrogel scaffold (AMG).

We incorporated exosomes derived from RBMSCs into the AMG pre-gel solution, resulting in the formation of exosome-loaded composite hydrogel scaffolds (Exo-AMG) through photocrosslinking. Fig. 4K illustrated the three-dimensional spatial distribution of DiI fluorescent dye-labeled exosomes in Exo-AMG hydrogels, confirming successful loading

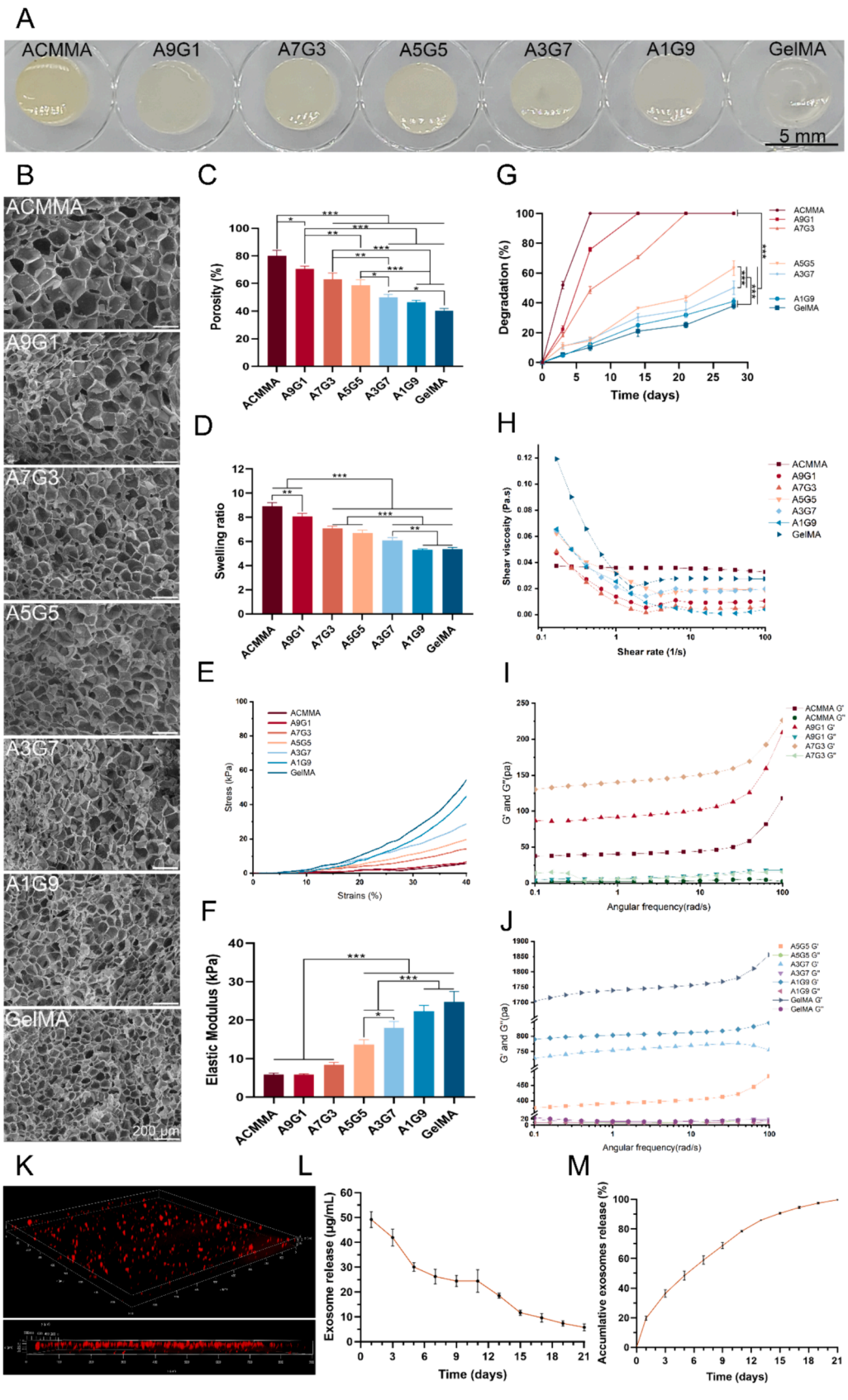

(caption on next page)

Fig. 4. Characterization of composite hydrogels. (A) Macroscopic appearance of ACMMA-GelMA composite hydrogel scaffold constructs with varying concentrations. (B) Scanning Electron Microscopy (SEM) images depicting the cross-section of hydrogel scaffolds with different concentrations. (C) The porosity of composite hydrogels in each group. (D) Assessment of the swelling properties of composite hydrogels. (E) The compressive stress–strain curve, (F) elastic modulus, and (G) degradation ratio of composite hydrogels in each group. (H), (I), and (J) Analysis of the rheological and mechanical properties of composite hydrogels with varying ACMMA compositions. (K) 3D image of Exo labeled with Dil in AMG hydrogel. (L) Presentation of the release curve and (M) the cumulative release profile of Exo-AMG hydrogel over a span of 21 days. Data expressed as mean ± SD (n = 3). *p < 0.05, **p < 0.01, ***p < 0.001.

and uniform dispersion of exosomes in the AMG hydrogel. More importantly, we explored the *in vitro* release behavior of the Exo-AMG scaffold (Fig. 4L and M). Analysis of the *in vitro* release curves and cumulative release curves of exosomes revealed a burst release phenomenon, with the exosome concentration in the eluate reaching approximately 49.18 ± 3.22 μg/ml on the first day, exhibiting a release rate of approximately 19.67 ± 1.29 %. This initial burst release may be caused by the composite hydrogel's stability. Addressing this issue is a priority in our future work. In summary, the exosomes in the Exo-AMG hydrogel scaffold exhibited sustained release over 21 days, and 90.57 ± 0.57 % of them were released by day 15. This ensured the optimal biological effects for chondral regeneration [19].

3.4. Biocompatibility of composite hydrogels in vitro

The growth plate primarily comprises transparent cartilage, making the biocompatibility of the filling material a crucial prerequisite for treating growth plate injuries [42]. To evaluate the biocompatibility of

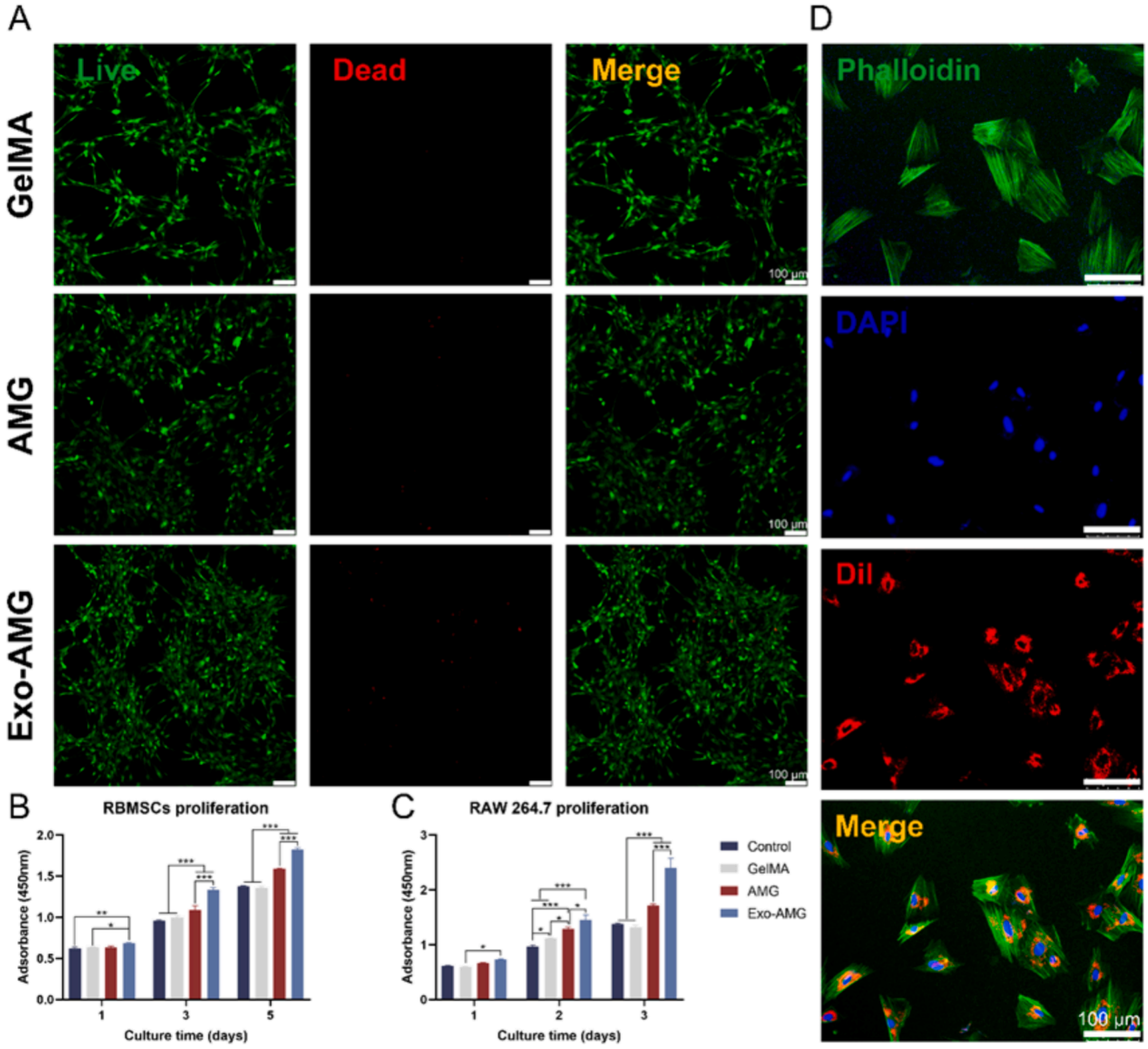

Fig. 5. Biocompatibility assessment of each group. (A) Live/Dead analysis conducted after 3 days of cell culture in each group. Green-stained cells (AM) represent live cells, while red-stained cells (PI) indicate dead cells. (B) The CCK-8 assay was performed at 1, 3, and 5 days of cell culture to measure cellular viability in each group. (C) The cellular viability of RAW 264.7 cells in each group was assessed using the CCK-8 assay. (D) After 12 h of co-incubation with fluorescently labeled exosomes, the internalization of exosomes by RBMSCs was visualized via laser confocal scanning microscopy. Data expressed as mean ± SD (n = 3). *p < 0.05, **p < 0.01, ***p < 0.001.

the composite hydrogels, RBMSCs were co-cultured with the hydrogels from each group. After 3 days of co-culture, the hydrogel scaffolds containing RBMSCs were underwent Live/Dead staining while the cell viability on the scaffolds was observed using a confocal laser scanning microscope (green for live and red for dead). As shown in Fig. 5A, RBMSCs cultured on the surfaces of hydrogels in all groups displayed a spindle-shaped morphology, with predominantly live cells and only a few instances of cell death. This shows the excellent cell viability, proving the outstanding biocompatibility across all hydrogel groups. The particularly noteworthy is the Exo-AMG group had the widest spreading area in the three groups, forming a sheet-like structure. RAW264.7 cells also adhered to the surface of each hydrogel group, especially the Exo-AMG group showing the largest cell distribution area after three days of co-culture (Fig. S4). The results of material characterization indicated that Exo-AMG possesses high hydrophilicity and an interconnected porous structure. After cell inoculation onto the surface of Exo-AMG hydrogel trays for culture, the images revealed cell proliferation and migration into the hydrogel as the material degrades, demonstrating that Exo-AMG can provide a three-dimensional microenvironment conducive to cell growth (Fig. S5).

Then, we assessed the impact of hydrogels on RBMSCs proliferation using the CCK-8 assay on the day 1, 3, and 5 of co-culture (Fig. 5B). There were no statistically significant differences in RBMSCs activity among the groups on day 1. As the culture time increasement, RBMSCs activity improved. On days 3 and 5, the RBMSCs activity in the AMG and Exo-AMG groups were higher than those in the Control and GelMA groups, and the Exo-AMG group exhibited significantly higher activity than the one in the AMG group. This indicates that ACMMA and exosomes have good biological activity in promoting RBMSCs proliferation. Additionally, we investigated the influence of hydrogels from various groups on the proliferation activity of RAW 264.7 macrophage cells. The results showed that the Exo-AMG group had the highest viability, and the viability of RAW 264.7 in the AMG group higher than the one in the Control and GelMA groups. This indicates a proliferation trend consistent with RBMSCs (Fig. 5C). ACMMA derived from cartilage contains a large number of endogenous components, such as chondroitin sulfate (CS), which has been shown to participate in various signaling pathways to promote RBMSCs proliferation. The exosomes from RBMSCs can also promote cell migration and proliferation with reducing apoptosis via the AKT and ERK signaling pathways [43,44]. In summary, the Exo-AMG hydrogel scaffold exhibited high biocompatibility, and the endogenous components showed a good proliferative effect on RBMSCs and RAW 264.7 cells.

To observe whether the exosomes loaded into Exo-AMG could be internalized by allogeneic cells, we labeled extracted exosomes with DiI dye (red fluorescence) and mixed them with the AMG pre-polymer solution to prepare hydrogel scaffolds. These scaffolds were then immersed in α-MEM complete culture medium in the dark. After co-culturing the eluate with logarithmically growing allogeneic RBMSCs in the dark, the FITC-phalloidin and DAPI were used to label the actin skeleton and cell nuclei, respectively. Confocal laser scanning microscopy (CLSM) was employed to observe the exosome internalization by RBMSCs. All the RBMSCs showed a large amount of red fluorescence signal in the cytoplasm (Fig. 5D), proving the allogeneic cells had uptake of exosomes loaded into Exo-AMG, thereby exerting their biological functions.

3.5. *Exo-AMG induce anti-inflammatory and macrophage M2 polarization in vitro*

Based on the current finding from a previous study, it has been observed that the growth plate injuries progress through four distinct stages: the inflammatory phase, fibrous tissue formation phase, ossification phase, and remodeling phase [45]. After a growth plate injury, the macrophages, serving as immune cells, can swiftly infiltrate the injury site within 8 h [46]. They undergo polarization into M1-type macrophages, secreting an abundance of pro-inflammatory factors [47]. This initiation of a local inflammatory response plays a pivotal role in regulating subsequent processes, ultimately culminating in bone bridging [48]. In this context, an *in vitro* study was conducted to investigate the impact of the Exo-AMG hydrogel on macrophage polarization.

Initially, the CCK-8 assay was employed to assess the impact of exosomes on RBMSCs proliferation, and the optimal concentration was determined as the positive control group. The results (refer to Fig. S6) revealed the strongest proliferation of RBMSCs between 25 μg/mL and 100 μg/mL of exosome concentration on the first and third days. However, by the fifth day, the proliferation capacity at 100 μg/mL was weaker than the groups from the 25 μg/mL to 75 μg/mL, with no statistically significant difference among the groups of 25 μg/mL, 50 μg/mL, and 75 μg/mL. Subsequently, the exosome concentration of 25 μg/mL was selected as the control group for subsequent experiments, named Exo.

To explore the inhibitory effect of the Exo-AMG hydrogel on inflammatory factors and its influence on macrophage phenotypes *in vitro*, we performed RT-qPCR analysis of the relevant inflammatory factors. The RAW 264.7 with Exo-AMG hydrogel for 3 days showed a reduction in mRNA expression levels of pro-inflammatory factors (IL-1β, IL-6, iNOS, and TNF-α) and the increase of serval anti-inflammatory factors (IL-1Ra, IL-10, Arg-1, and TGF-β) (Fig. 6A and B). This trend became more pronounced by the 5th day of culture (Fig. 6D and E). Notably, the capacity of Exo alone on the reduction of pro-inflammatory factor expression and induction of anti-inflammatory factor expression was greater than that of Exo-AMG. This phenomenon may be due to the unstable release rate of exosomes in Exo-AMG, and this is an issue to be addressed in our future work.

Western blot (WB) was employed to directly observe the expression of M2 macrophage marker CD206 and M1 macrophage marker CD86, further confirming the ability of the Exo-AMG hydrogel to promote M2 polarization in macrophages. Compared to the control group, the expression levels of CD206 on the 3rd day and 5th day were 1.32 and 1.83 times in the Exo-AMG group (Fig. 6C and G), and the expression of CD86 were 0.53 and 0.71 times, respectively (Fig. 6F and H). Subsequently, RAW 264.7 cells were seeded on each hydrogel sample, and LPS (100 ng/ml) was added to the culture medium. After 5 days of co-culture, RT-qPCR confirmed the immunomodulatory properties of the Exo-AMG hydrogel under pro-inflammatory conditions, with significantly lower expression of pro-inflammatory factors and higher expression of anti-inflammatory factors compared with the control group (Fig. 6 I and J).

According to the previous studies, exosome is highly functional in molecular immunity regulation. It envelops mRNA, miRNA, cytokines and chemokines, which play an important role in regulating the phenotype and function of immune cells [49]. The exosome derived from RBMSCs contains bioactive molecules, especially miR-199a, which regulates immune cell M2 polarization via inhibiting the NF-κB pathway. This may contribute to growth plate repair [49]. M1 macrophages secrete pro-inflammatory mediators and stroma-degrading enzymes, which exacerbate the inflammatory environment, trigger apoptosis of chondrocytes, and disrupt the balance between the synthesis and decomposition of new cartilage [42,50]. As the cartilage structure gradually disappears, inflammatory cells invade and blood vessels grow in, eventually forming bone bridges [51,52]. Based on these, our Exo-AMG hydrogel can continuously release exosomes in the early stage of growth plate injury, regulate the polarization of macrophages, alleviate the inflammatory reaction process, block subsequent pathological changes, curb cartilage injury and bone bridge formation at the source, and reduce pain, all of which could benefit the promotion the regeneration and repair of growth plate cartilage injury.

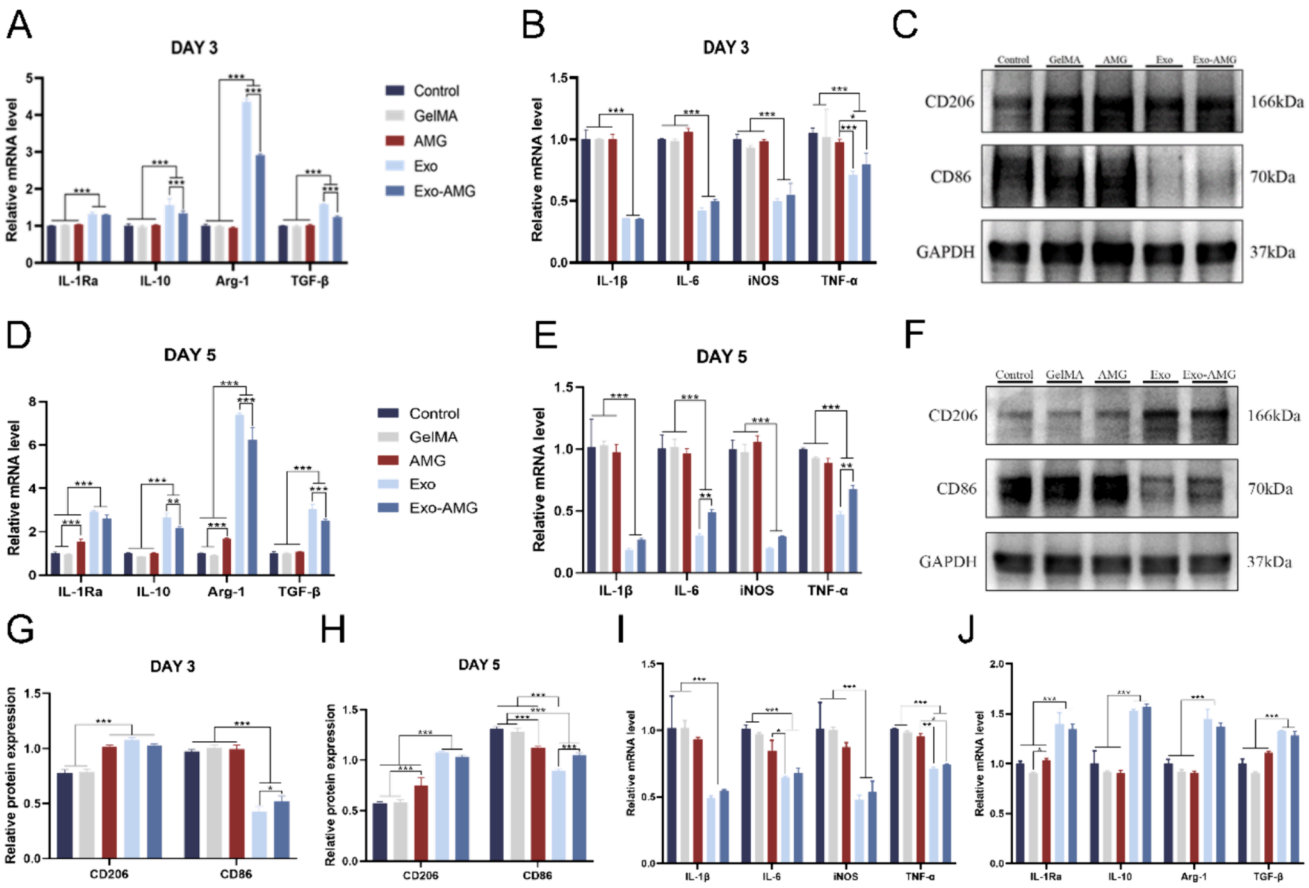

Fig. 6. Effects of Exo-AMG hydrogel on anti-inflammatory response and macrophage M2 polarization. (A-B) Following three days of co-culture, mRNA expression levels of anti-inflammatory and proinflammatory cytokines were assessed in each group. (C) After the three-day co-culture period, Western Blot analysis was performed on CD206 and CD86 protein bands in each group. (D-E) Subsequent to five days of co-culture, mRNA expression levels of anti-inflammatory and proinflammatory cytokines were evaluated in each group. (F) Following the five-day co-culture, Western Blot analysis was conducted on the CD206 and CD86 protein bands in each group. (G-H) Quantitative analysis of the CD206 and CD86 protein expression in each group was conducted. (I-J) mRNA expression levels of anti-inflammatory and proinflammatory cytokines in each group were assessed in a proinflammatory medium. Data expressed as mean ± SD (n = 3). *p < 0.05, **p < 0.01, ***p < 0.001.

3.6. Exo-AMG promote migration and chondrogenic differentiation of RBMSCs in vitro

We conducted Transwell chamber experiments to validate the influence of Exo-AMG on RBMSCs migration *in vitro*. Crystal violet-stained images clearly demonstrated an increased number of migrating cells on the lower surface of the insert after 24 h of the RBMSCs exposure to the Exo-AMG hydrogel extract (Fig. 7A). The cell amount in each group revealed that the Exo-AMG group exhibited approximately 2575.67 ± 308.73 migrating cells, showing no significant difference from the Exo group, but significantly surpassed that of the other groups (Fig. 7C). These findings demonstrate that the Exo-AMG hydrogel could significantly promote cell migration by releasing exosomes into the medium. Interestingly, it exhibited a higher number of migrated cells in the AMG group than the numbers in the Control and GelMA groups. We postulate that the AMG hydrogel scaffold could maintain the necessary microenvironment for RBMSCs, utilizing its original components to guide and regulate the functions of surrounding cells.

To evaluate the impact of Exo-AMG hydrogel scaffolds on the chondroid differentiation of RBMSCs, the cells were cultured with the induced extract of hydrogel cartilage differentiation in each group. The cartilage matrix produced by RBMSCs in each group was assessed through toluidine blue staining images after 3 weeks (Fig. 7B). Toluidine blue, a quinone imide alkaline dye, forms salt bonds with cations in tissues' carboxylic groups, resulting in a light blue coloration of acidic mucous substances, such as glycosaminoglycans [53]. The depth of toluidine blue staining correlates with the extent of the cartilaginous extracellular matrix, indicating successful chondrogenic differentiation of RBMSCs. In comparison with the Control, GelMA and AMG group, the Exo-AMG group and Exo group exhibited a superior chondrogenic effect, characterized by the presence of round chondroid cells and cartilage lacunar-like structures. Macroscopically, the addition of Exo and ACMMA components demonstrated the promotion of chondroid differentiation in RBMSCs, highlighting the potential of Exo-AMG hydrogel scaffolds as a promising approach for repairing damaged growth plates.

To validate the chondrogenic differentiation potential of Exo-AMG on RBMSCs, we assessed the expression of key chondrogenic genes (SOX9, COL II, ACAN, and PRG4) and osteogenesis-related genes (OCN, OPN, COL I, and ALP) at the gene level (Fig. 7D and E). RT-qPCR results revealed a significant upregulation of chondrogenic genes in both the Exo and Exo-AMG groups. Moreover, in the AMG group, there was a higher expression of chondrogenic genes than the expressions in the Control and GelMA groups. Conversely, the expression levels of osteogenic genes in the AMG and Exo-AMG groups were lower, while the Exo group displayed a significant increase. These findings shows that RBMSCs-derived exosomes upregulate both chondrogenic and osteogenic genes. The exosomes encapsulating microRNAs, mRNAs, and various biological factors actively participate in the regulation of a range of physiological processes, including signaling pathways [21,54]. They play a pivotal role in promoting the repair and potential multidirectional differentiation of stem cells [55–57]. The elevated expression of chondrogenic genes and diminished expression of osteogenic

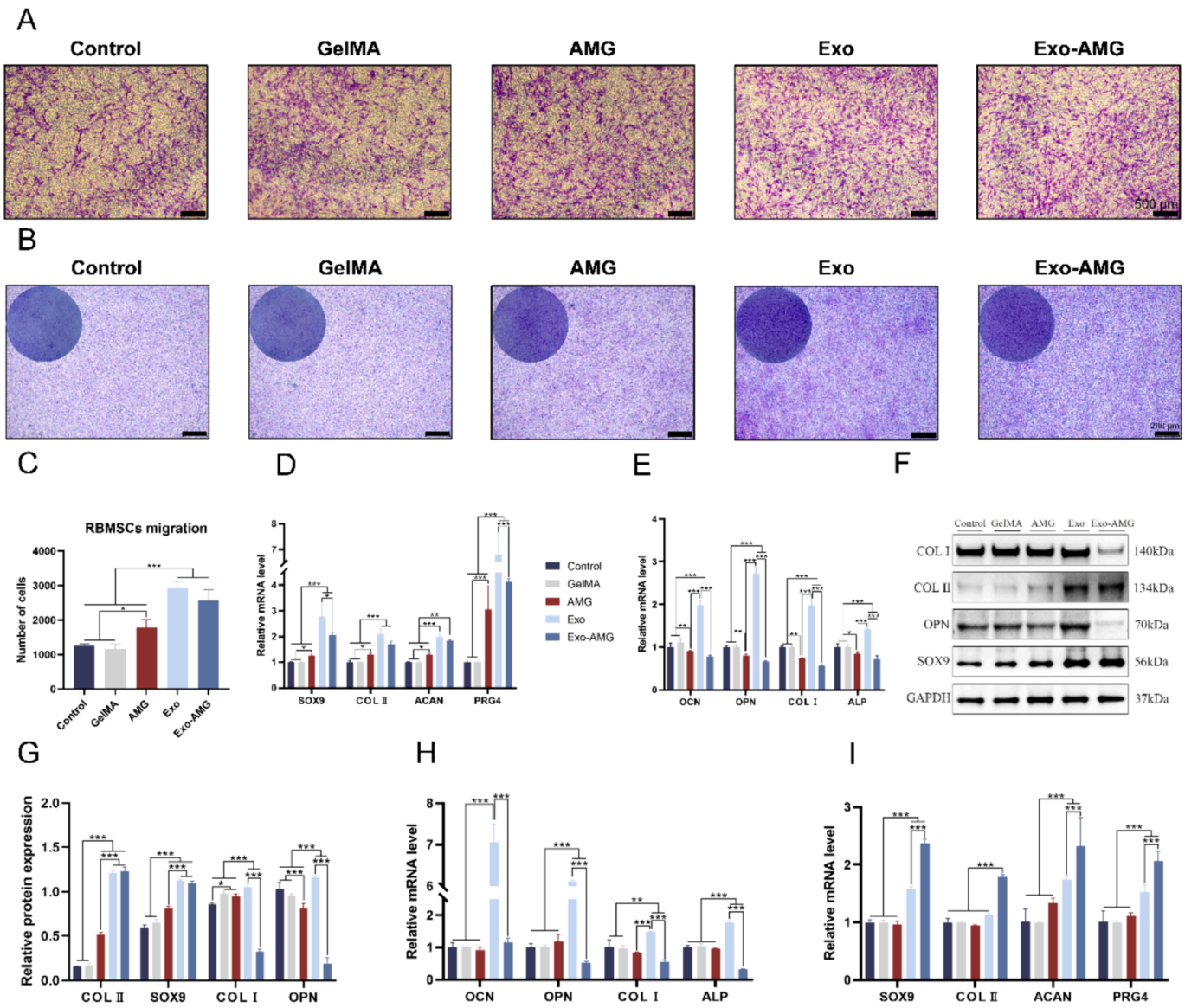

Fig. 7. Effects of Exo-AMG hydrogel on cellular behavior and cartilage differentiation.(A) Crystalline violet staining and (C) semi-quantitative results from Transwell chambers after 12 h of co-culture.(B) Representative images from Toluidine blue staining depict the composite hydrogels in each group after 3 weeks of culture.(D-E) RT-PCR analysis was conducted to assess the expression of chondrogenesis-related and osteogenic-related genes.(F) Western Blot analysis was performed to examine the protein bands of COL I, COL II, OPN, and SOX9 in each group.(G) Quantitative analysis of the protein expression levels of COL I, COL II, OPN, and SOX9 in each group.(H-I) RT-PCR analysis was carried out to evaluate the expression of chondrogenesis-related and osteogenic-related genes in an osteogenic medium. Data expressed as mean ± SD (n = 3). *p < 0.05, **p < 0.01, ***p < 0.001.

genes in the AMG and Exo-AMG groups can be attributed to the incorporation of ACMMA. Some previous studies have demonstrated that ACMMA derived from cartilage sources is rich in active proteins and growth factors, effectively guiding chondrogenic differentiation by altering the stem cell growth microenvironment [58]. The superior ability of Exo-AMG to promote chondrogenic differentiation and suppress osteogenic differentiation compared to the AMG group. This suggests an amplification of these effects via the exosomes loading in the Exo-AMG group, which synergistically induces RBMSCs toward chondrocyte differentiation. SOX9, a key transcription factor in cartilage formation, regulates the expression of cartilage-related markers (type collagen II) and the formation of GAG matrix [59]. The WB results (Fig. 7F and G) demonstrated that the expression levels of SOX9 and COL II in the Exo-AMG group were 1.84 and 8.05 times higher than those in the Control group, while the expression levels of OPN and COL I were 0.18 and 0.38 times, respectively, consistent with RT-qPCR results.

Finally, the RBMSCs were cultured on the surfaces of hydrogels in each group, and after 14 days of culture in osteogenic induction extract, RT-qPCR was employed to quantitatively analyze the expression of chondrogenic and osteogenic genes (Fig. 7H and I). In the pro-osteogenic microenvironment, the Exo group exhibited significantly higher expression of osteogenic-related genes than the expressions in the other groups but still maintained a certain ability to promote chondrogenic differentiation in RBMSCs. The Exo-AMG group continued to show an upregulation trend in chondrogenic marker genes and a down-regulation trend in osteogenic marker genes, highlighting the crucial role of the microenvironment influenced by ACMMA in the ability of exosomes to exhibit osteogenic or chondrogenic potential.

In summary, the Exo-AMG composite hydrogel scaffold could not only provide structural support for cell adhesion and growth but also maintain a microenvironment conducive to cartilage regeneration, through the degradation of cartilage-derived components and the sustained release of exosomes. This microenvironment recruits adherent bone marrow mesenchymal stem cells and guides the modulation of

surrounding cell functions, including stem cell proliferation and differentiation. It directly promotes the remodeling of the chondrocyte extracellular matrix, offering unparalleled advantages in the repair of growth plate tissue structures. However, we only investigated phenotypic changes such as cell proliferation and differentiation. Further exploration of Exo-AMG's specific mechanisms in growth plate cartilage regeneration through *in vitro* studies remains a focus of future research.

3.7. Growth plate regeneration performance in vivo

The surgical procedure for growth plate injury and subsequent hydrogel implantation is depicted in Fig. 8A. Histological assessments of tibial growth plate defect samples at 1 month and 3 months post-surgery offered insights into the regenerative capacities of each group (Fig. 8B). H&E staining illustrated that the center of the growth plate was successfully interrupted in all groups, confirming the establishment of the tibial growth plate injury model. The results of comparative analysis revealed that, in contrast in the Control groups, GelMA, AMG, the rabbits in the Exo-AMG groups exhibited conspicuous cartilage regeneration within the injured area. Specifically, the rabbits of the Control group exhibited significant structural collapse and angular distortion at the injury site while in the AMG and Exo-AMG groups the rabbits displayed milder or no distortion. This demonstrates that the injectable hydrogel, following *in situ* photocrosslinking, effectively filled the defect area, provided mechanical support, and facilitated the repair of the growth plate injury. Minimal cartilage formation and distinct bone bridges were observed in the Control group. But in the AMG group it showed reduced bone bridge formation and the initiation of the cartilage regeneration. In contrast, in the Exo-AMG group, the significant and continuous cartilage regeneration was observed, with less bone tissue formation. The regenerated cartilage displayed a continuous and regular morphology, closely resembling the undamaged growth plate cartilage. Consistent with H&E staining, AB and TB staining confirmed minimal cartilage formation in the Control and GelMA groups, atypical cartilage regeneration in the AMG group, and the least bone bridge formation in the Exo-AMG group (Fig. 8C and D).

Notably, the Exo-AMG group exhibited evident circular chondrocytes and a restored a three-layered functional zone, encompassing the resting zone, proliferative zone, and hypertrophic zone. This is crucial for growth plate function, as the coordinated work of these zones contributes to the development of the growth plate [60]. In the resting zone, chondroprogenitor cells transition from a quiescent state to the proliferative zone, forming a columnar arrangement crucial for skeletal growth [61]. In the hypertrophic zone, chondrocytes cease proliferation, enlarge, and produce type X collagen, leading to matrix mineralization. Chondrocytes in this zone may undergo apoptosis or transform into osteoblasts, facilitating cartilage-to-bone transition and skeletal growth [8].Throughout this process, chondrocytes transition from a resting state to a hypertrophic state, followed by calcification and vascular invasion, leading to bone formation [58]. The local cartilage microenvironment within the body plays a crucial role in determining the fate of stem cell differentiation and the type of regenerated cartilage [62].

As highlighted earlier, the conventional filling materials used in clinical settings for growth plate injuries often fail to achieve regenerative repair of the growth plate defect sites. The Exo-AMG hydrogel, through its unique properties, not only fills the defect area, providing mechanical support and limiting bone bridge formation but also promotes growth plate cartilage-specific regeneration by inhibiting local bone repair through the degradation of its own decellularized cartilage matrix and the localized release of exosomes. This represents a significant advancement in achieving regeneration of cartilage tissue structure and function in growth plate injuries.

Although the Exo-AMG demonstrates promising activity in repairing growth plate cartilage, our study still has limitations. When dealing with extensive growth plate injuries or even fractures, the repairing not only for the growth plate cartilage but also for the surrounding metaphyseal bone layers becomes more necessary. In terms of bone tissue repair, the Exo-AMG exhibits weaker mechanical properties and a faster degradation rate, making it challenging to provide sustained support to the defect area. In future research, combining computer-aided design with 3D printing technology can be considered to construct biphasic gradient hydrogel scaffolds tailored to specific injury ranges. By designing multilayered hydrogel scaffolds with different microcomponents and microstructures, we can better mimic the specific microenvironments required for cartilage and bone repair, thereby achieving regeneration of both the growth plate cartilage and surrounding metaphyseal bone tissue. In addition to tissue section staining, experiments such as gait analysis, imaging analysis, and transcriptomic analysis will be performed to further explore the performance and mechanisms of biomaterials in restoring normal tissue physiological functions.

4. Conclusion

This study employed the exosomes derived from RBMSCs, cartilage-derived ACMMA material, and GelMA to fabricate an injectable composite hydrogel. This hydrogel demonstrated the ability to rapidly crosslink, forming a stable three-dimensional network structure under UV irradiation at a wavelength of 405 nm. This feature renders it highly suitable for repairing and regenerating growth plate cartilage following trauma. Both *in vitro* and *in vivo* experiments confirmed that the hydrogel provides a conducive three-dimensional microenvironment, closely resembling the extracellular matrix components of cartilage, with appropriate mechanical properties and excellent biocompatibility. Through the sustained release of exosomes and ACMMA degradation, Exo-AMG enhanced the local microenvironment, suppressed early inflammatory reactions and bone repair, promoted BMSCs proliferation, and guided differentiation towards chondrogenesis. This facilitated the remodeling of the extracellular matrix of chondrocytes in the injured area, ultimately leading to successful cartilage regeneration. Therefore, the Exo-AMG hydrogel emerges as a promising candidate for promoting cartilage regeneration after growth plate injury while simultaneously preventing bone bridge formation.

Funding

This work was supported by Jiangsu Provincial Key Research and Development Program (CN) (grant number BE2019608); Postdoctoral Research Foundation of China (2022M721685); Jiangsu Health Commission Medical Research Program (grant number 2020158); National Facility for Translational Medicine (Shanghai) Open Program (grant number TMSK-2021-304); Nanjing International Science and Technology Cooperation Program; Nanjing Medical Science and Technology Development Key Program (grant number ZKX18041); Nanjing Postdoctoral Research Funding Program.

CRediT authorship contribution statement

Xinxin Si: Supervision, Formal analysis, Conceptualization. **Quan Zhang:** Writing – original draft, Methodology, Data curation, Conceptualization. **Bo Ning:** Validation, Methodology, Conceptualization. **Lei Qiang:** Writing – original draft, Methodology, Formal analysis, Conceptualization. **Qiang Li:** Formal analysis, Data curation. **Yihao Liu:** Supervision, Methodology. **Minjie Fan:** Formal analysis, Data curation. **Jing Shan:** Methodology, Investigation. **Guanlu Shen:** Validation, Methodology. **Zichen Lin:** Validation, Methodology. **Pengfei Zheng:** Writing – review & editing, Supervision, Funding acquisition, Formal analysis, Conceptualization.

Declaration of competing interest

The authors declare that they have no known competing financial interests or personal relationships that could have appeared to influence

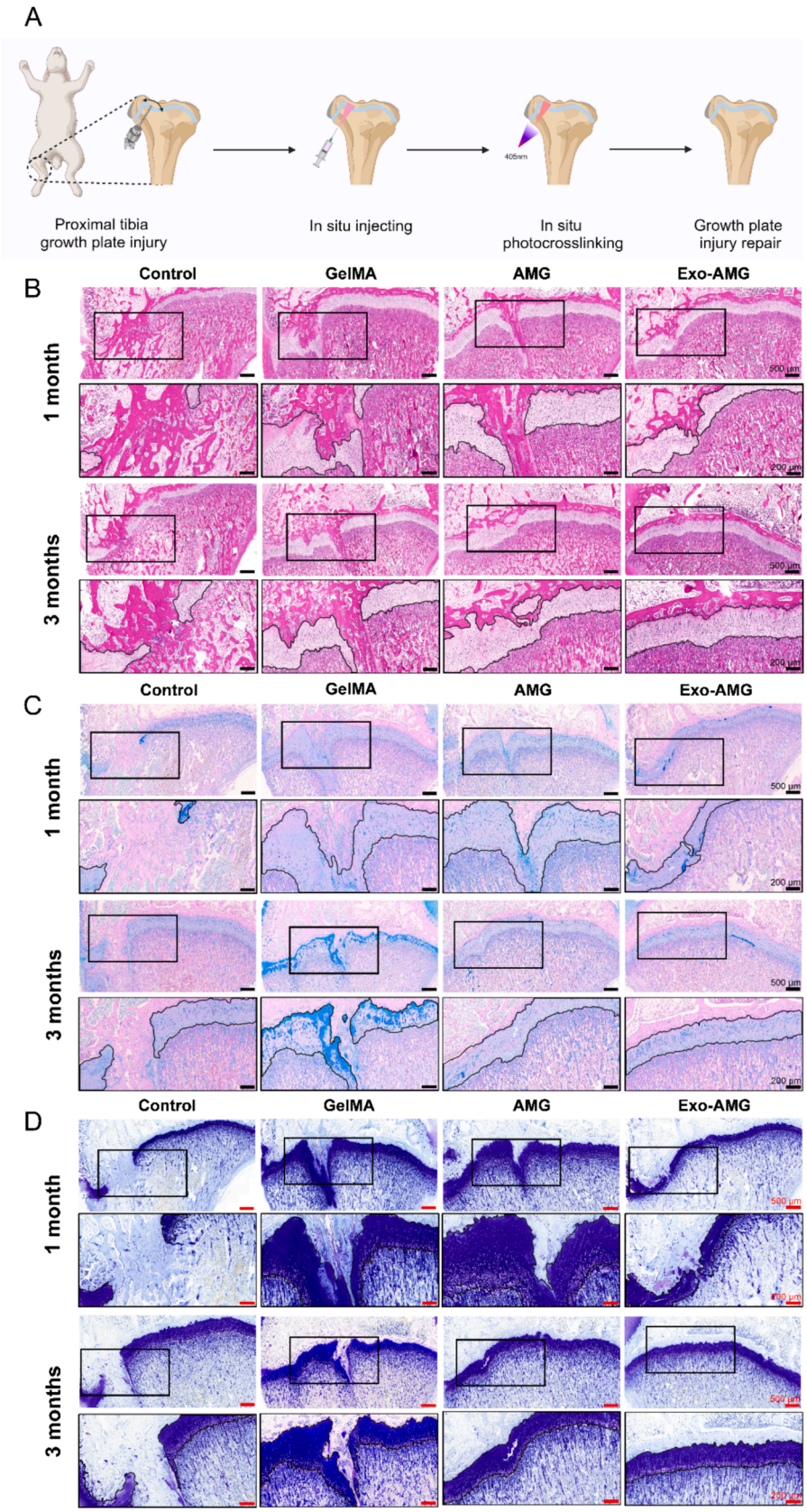

Fig. 8. Exo-AMG stimulate the repair of growth plates after injury and diminishes bone bridge formation. (A) Illustration of the surgical procedure performed on the rat femur drill model. Staining images, including H&E (B), AB (C), and TB (D), were captured at the injury site in the growth plate. The scale bar of 500 μm is employed to denote the original magnification. The boxed area, symbolizing the defect site, is additionally magnified and presented below with a scale bar of 200 μm. The region demarcated by black lines predominantly represents the growth plate cartilage.

the work reported in this paper.

Data availability

Data will be made available on request.

Acknowledgements

The authors would like to acknowledge the creation of Scheme 1, Fig. 2A, Fig. 3A, and Fig. 8A, which were generated using biorender.com.

Appendix A. Supplementary data

Supplementary data to this article can be found online at https://doi.org/10.1016/j.cej.2024.152463.

References

[1] P.T. Newton, L. Li, B. Zhou, C. Schweingruber, M. Hovorakova, M. Xie, X. Sun, L. Sandhow, A.V. Artemov, E. Ivashkin, S. Suter, V. Dyachuk, M. El Shahawy, A. Gritli-Linde, T. Bouderlique, J. Petersen, A. Mollbrink, J. Lundeberg, G. Enikolopov, H. Qian, K. Fried, M. Kasper, E. Hedlund, I. Adameyko, L. Sävendahl, A.S. Chagin, A radical switch in clonality reveals a stem cell niche in the epiphyseal growth plate, Nature 567 (7747) (2019) 234–238.
[2] J.B. Samora, Distal radius physeal bar and ulnar overgrowth: indications for treatment, J. Pediatr. Orthop. 41 (Suppl 1) (2021) S6–s13.
[3] C.B. Erickson, N. Shaw, N. Hadley-Miller, M.S. Riederer, M.D. Krebs, K.A. Payne, A rat tibial growth plate injury model to characterize repair mechanisms and evaluate growth plate regeneration strategies, J. Visual. Exp.: Jove 125 (2017).
[4] D.B. Fox, Physeal injuries and angular limb deformities, the veterinary clinics of North America, Small Animal Practice 51 (2) (2021) 305–322.
[5] G. Fu, W. Wang, Y.F. Dong, X.M. Lv, Z. Yang, Treatment of post-traumatic pediatric ankle varus deformity with physeal bar resection and hemi-epiphysiodesis, Curr. Med. Sci. 39 (4) (2019) 604–608.
[6] M. Karlikowski, J. Sułko, Physeal fractures of the lower leg in children and adolescents: Therapeutic results, pitfalls and suggested management protocol - based on the experience of the authors and contemporary literature, Adv. Med. Sci. 63 (1) (2018) 107–111.
[7] X. Wang, Z. Li, C. Wang, H. Bai, Z. Wang, Y. Liu, Y. Bao, M. Ren, H. Liu, J. Wang, Enlightenment of growth plate regeneration based on cartilage repair theory: A review, Front. Bioeng. Biotechnol. 9 (2021).
[8] N. Shaw, C. Erickson, S.J. Bryant, V.L. Ferguson, M.D. Krebs, N. Hadley-Miller, K. A. Payne, Regenerative medicine approaches for the treatment of pediatric physeal injuries, Tissue Eng. B Rev. 24 (2) (2017) 85–97.
[9] X. Wang, Z. Li, C. Wang, H. Bai, Z. Wang, Y. Liu, Y. Bao, M. Ren, H. Liu, J. Wang, Enlightenment of growth plate regeneration based on cartilage repair theory: A review, Front. Bioeng. Biotechnol. 9 (2021) 654087.
[10] Ž. Večerić-Haler, A. Cerar, M. Perše, (Mesenchymal) stem cell-based therapy in cisplatin-induced acute kidney injury animal model: risk of immunogenicity and tumorigenicity, Stem Cells Int. 2017 (2017) 7304643.
[11] L. Barkholt, E. Flory, V. Jekerle, S. Lucas-Samuel, P. Ahnert, L. Bisset, D. Büscher, W. Fibbe, A. Foussat, M. Kwa, O. Lantz, R. Mačiulaitis, T. Palomäki, C.K. Schneider, L. Sensebé, G. Tachdjian, K. Tarte, L. Tosca, P. Salmikangas, Risk of tumorigenicity in mesenchymal stromal cell-based therapies–bridging scientific observations and regulatory viewpoints, Cytotherapy 15 (7) (2013) 753–759.
[12] N. Heldring, I. Mäger, M.J. Wood, K. Le Blanc, S.E. Andaloussi, Therapeutic potential of multipotent mesenchymal stromal cells and their extracellular vesicles, Hum. Gene Ther. 26 (8) (2015) 506–517.
[13] W. Guo, W. Xu, Z. Wang, M. Chen, C. Hao, X. Zheng, J. Huang, X. Sui, Z. Yuan, Y. Zhang, M. Wang, X. Li, Z. Wang, J. Peng, A. Wang, Y. Wang, S. Liu, S. Lu, Q. Guo, Cell-free strategies for repair and regeneration of meniscus injuries through the recruitment of endogenous stem/progenitor cells, Stem Cells Int. 2018 (2018) 5310471.
[14] S. Kourembanas, Exosomes: vehicles of intercellular signaling, biomarkers, and vectors of cell therapy, Annu. Rev. Physiol. 77 (2015) 13–27.
[15] W. Li, L.Y. Jin, Y.B. Cui, N. Xie, Human umbilical cord mesenchymal stem cells-derived exosomal microRNA-17-3p ameliorates inflammatory reaction and antioxidant injury of mice with diabetic retinopathy via targeting STAT1, Int. Immunopharmacol. 90 (2021) 107010.
[16] C. Zhang, Z. Zhu, J. Gao, L. Yang, E. Dang, H. Fang, S. Shao, S. Zhang, C. Xiao, X. Yuan, W. Li, R. Abe, H. Qiao, G. Wang, M. Fu, Plasma exosomal miR-375-3p regulates mitochondria-dependent keratinocyte apoptosis by targeting XIAP in severe drug-induced skin reactions, Sci. Transl. Med. 12 (574) (2020).
[17] Y. Zhang, J. Zhao, M. Ding, Y. Su, D. Cui, C. Jiang, S. Zhao, G. Jia, X. Wang, Y. Ruan, Y. Jing, S. Xia, B. Han, Loss of exosomal miR-146a-5p from cancer-associated fibroblasts after androgen deprivation therapy contributes to prostate cancer metastasis, J. Exp. Clin. Cancer Res.: CR 39 (1) (2020) 282.
[18] S. Keshtkar, N. Azarpira, M.H. Ghahremani, Mesenchymal stem cell-derived extracellular vesicles: novel frontiers in regenerative medicine, Stem Cell Res. Ther. 9 (1) (2018) 63.
[19] P. Guan, C. Liu, D. Xie, S. Mao, Y. Ji, Y. Lin, Z. Chen, Q. Wang, L. Fan, Y. Sun, Exosome-loaded extracellular matrix-mimic hydrogel with anti-inflammatory property Facilitates/promotes growth plate injury repair, Bioact. Mater. 10 (2022) 145–158.
[20] D.M. Pegtel, S.J. Gould, Exosomes, Annu. Rev. Biochem. 88 (2019) 487–514.
[21] S. Zhang, W.C. Chu, R.C. Lai, S.K. Lim, J.H. Hui, W.S. Toh, Exosomes derived from human embryonic mesenchymal stem cells promote osteochondral regeneration, Osteoarthr. Cartil. 24 (12) (2016) 2135–2140.
[22] W. Lu, J. Xu, S. Dong, G. Xie, S. Yang, X. Huangfu, X. Li, Y. Zhang, P. Shen, Z. Yan, H. Liu, Z. Deng, J. Zhao, Anterior Cruciate ligament reconstruction in a rabbit model using a decellularized allogenic semitendinous tendon combined with autologous bone marrow-derived mesenchymal stem cells, Stem Cells Transl. Med. 8 (9) (2019) 971–982.
[23] V. Moreno-Manzano, D. Zaytseva-Zotova, E. López-Mocholí, Á. Briz-Redón, B. Løkensgard Strand, Á. Serrano-Aroca, Injectable gel form of a decellularized bladder induces adipose-derived stem cell differentiation into smooth muscle cells in vitro, Int. J. Mol. Sci. 21 (22) (2020).
[24] K.E.M. Benders, M.L. Terpstra, R. Levato, J. Malda, Fabrication of decellularized cartilage-derived matrix scaffolds, J. Visual. Exp.: Jove 143 (2019).
[25] W. Li, R. Xu, J. Huang, X. Bao, B. Zhao, Treatment of rabbit growth plate injuries with oriented ECM scaffold and autologous BMSCs, Sci. Rep. 7 (2017) 44140.
[26] L. Jia, Y. Zhang, L. Yao, P. Zhang, Z. Ci, W. Zhang, C. Miao, X. Liang, A. He, Y. Liu, S. Tang, R. Zhang, X. Wang, Y. Cao, G. Zhou, Regeneration of human-ear-shaped cartilage with acellular cartilage matrix-based biomimetic scaffolds, Appl. Mater. Today 20 (2020) 100639.
[27] X. Nie, Y.J. Chuah, W. Zhu, P. He, Y. Peck, D.A. Wang, Decellularized tissue engineered hyaline cartilage graft for articular cartilage repair, Biomaterials 235 (2020) 119821.
[28] L. Jia, Y. Hua, J. Zeng, W. Liu, D. Wang, G. Zhou, X. Liu, H. Jiang, Bioprinting and regeneration of auricular cartilage using a bioactive bioink based on microporous photocrosslinkable acellular cartilage matrix, Bioact. Mater. 16 (2022) 66–81.
[29] R. Guo, H. Zhuang, X. Chen, Y. Ben, M. Fan, Y. Wang, P. Zheng, Tissue engineering in growth plate cartilage regeneration: mechanisms to therapeutic strategies, J. Tissue Eng. 14 (2023), 20417314231187956.
[30] Z. Dong, Q. Yuan, K. Huang, W. Xu, G. Liu, Z. Gu, Gelatin methacryloyl (GelMA)-based biomaterials for bone regeneration, RSC Adv. 9 (31) (2019) 17737–17744.
[31] X. Yu, X. Wang, D. Li, R. Sheng, Y. Qian, R. Zhu, X. Wang, K. Lin, Mechanically reinforced injectable bioactive nanocomposite hydrogels for in-situ bone regeneration, Chem. Eng. J. 433 (2022) 132799.
[32] S. Jiang, G. Tian, Z. Yang, X. Gao, F. Wang, J. Li, Z. Tian, B. Huang, F. Wei, X. Sang, L. Shao, J. Zhou, Z. Wang, S. Liu, X. Sui, Q. Guo, W. Guo, X. Li, Enhancement of acellular cartilage matrix scaffold by Wharton's jelly mesenchymal stem cell-derived exosomes to promote osteochondral regeneration, Bioact. Mater. 6 (9) (2021) 2711–2728.
[33] J. He, Y. Sun, Q. Gao, C. He, K. Yao, T. Wang, M. Xie, K. Yu, J. Nie, Y. Chen, Y. He, Gelatin methacryloyl hydrogel, from standardization, performance, to biomedical application, Adv. Healthc. Mater. 12 (23) (2023) e2300395.
[34] L. Qiang, M. Fan, Y. Wang, Y. Liu, H. Zhuang, R. Guo, H. Huang, Y. Ben, D. Wang, X. Wu, J. Wang, J. Weng, P. Zheng, Injectable hydrogel loaded with bilayer microspheres to inhibit angiogenesis and promote cartilage regeneration for repairing growth plate injury, Front. Bioeng. Biotechnol. 11 (2023).
[35] Y. Sun, L. Yan, S. Chen, M. Pei, Functionality of decellularized matrix in cartilage regeneration: A comparison of tissue versus cell sources, Acta Biomater. 74 (2018) 56–73.
[36] Y. Zhang, J. Dai, L. Yan, Y. Sun, Intra-articular injection of decellularized extracellular matrices in the treatment of osteoarthritis in rabbits, PeerJ 8 (2020) e8972.
[37] N.K. Singh, W. Han, S.A. Nam, J.W. Kim, J.Y. Kim, Y.K. Kim, D.-W. Cho, Three-dimensional cell-printing of advanced renal tubular tissue analogue, Biomaterials 232 (2020) 119734.
[38] H. Kim, B. Kang, X. Cui, S.-H. Lee, K. Lee, D.-W. Cho, W. Hwang, T.B.F. Woodfield, K.S. Lim, J. Jang, Light-activated decellularized extracellular matrix-based bioinks for volumetric tissue analogs at the centimeter scale, Adv. Funct. Mater. 31 (32) (2021) 2011252.
[39] Y. Zhang, H. Leng, Z. Du, Y. Huang, X. Liu, Z. Zhao, X. Zhang, Q. Cai, X. Yang, Efficient regeneration of rat calvarial defect with gelatin-hydroxyapatite composite cryogel, Biomed. Mater. (Bristol England) 15 (6) (2020) 065005.
[40] S.H. Oh, D.B. An, T.H. Kim, J.H. Lee, Wide-range stiffness gradient PVA/HA hydrogel to investigate stem cell differentiation behavior, Acta Biomater. 35 (2016) 23–31.
[41] P. Guan, Y. Ji, X. Kang, W. Liu, Q. Yang, S. Liu, Y. Lin, Z. Zhang, J. Li, Y. Zhang, C. Liu, L. Fan, Y. Sun, Biodegradable Dual-Cross-Linked Hydrogels with Stem Cell Differentiation Regulatory Properties Promote Growth Plate Injury Repair via Controllable Three-Dimensional Mechanics and a Cartilage-like Extracellular Matrix, ACS applied materials & interfaces (2023).
[42] R. Chung, C.J. Xian, Mechanisms for growth plate injury repair and potential cell-based therapies for regeneration, J. Mol. Endocrinol. 53 (1) (2014) T45–T61.
[43] S. Chen, W. Chen, Y. Chen, X. Mo, C. Fan, Chondroitin sulfate modified 3D porous electrospun nanofiber scaffolds promote cartilage regeneration, Mater. Sci. Eng. C 118 (2021) 111312.
[44] S. Zhang, S.J. Chuah, R.C. Lai, J.H.P. Hui, S.K. Lim, W.S. Toh, MSC exosomes mediate cartilage repair by enhancing proliferation, attenuating apoptosis and modulating immune reactivity, Biomaterials 156 (2018) 16–27.

[45] M. Shen, S. Liu, X. Jin, H. Mao, F. Zhu, T. Saif, R. Zhou, H. Fan, P.C. Begeman, C. C. Chou, K.H. Yang, Porcine growth plate experimental study and estimation of human pediatric growth plate properties, J. Mech. Behav. Biomed. Mater. 101 (2020) 103446.
[46] B. Beamer, C. Hettrich, J. Lane, Vascular endothelial growth factor: an essential component of angiogenesis and fracture healing, HSS J. 6 (1) (2010) 85–94.
[47] H. Zhang, D. Cai, X. Bai, Macrophages regulate the progression of osteoarthritis, Osteoarthr. Cartil. 28 (5) (2020) 555–561.
[48] Y.W. Su, D.S.K. Wong, J. Fan, R. Chung, L. Wang, Y. Chen, C.H. Xian, L. Yao, L. Wang, B.K. Foster, J. Xu, C.J. Xian, Enhanced BMP signalling causes growth plate cartilage dysrepair in rats, Bone 145 (2021) 115874.
[49] L. Fan, P. Guan, C. Xiao, H. Wen, Q. Wang, C. Liu, Y. Luo, L. Ma, G. Tan, P. Yu, L. Zhou, C. Ning, Exosome-functionalized polyetheretherketone-based implant with immunomodulatory property for enhancing osseointegration, Bioact. Mater. 6 (9) (2021) 2754–2766.
[50] Y.B. Park, C.W. Ha, C.H. Lee, Y.C. Yoon, Y.G. Park, Cartilage regeneration in osteoarthritic patients by a composite of allogeneic umbilical cord blood-derived mesenchymal stem cells and hyaluronate hydrogel: results from a clinical trial for safety and proof-of-concept with 7 years of extended follow-up, Stem Cells Transl. Med. 6 (2) (2017) 613–621.
[51] M.J. Wood, A. Leckenby, G. Reynolds, R. Spiering, A.G. Pratt, K.S. Rankin, J. D. Isaacs, M.A. Haniffa, S. Milling, C.M. Hilkens, Macrophage proliferation distinguishes 2 subgroups of knee osteoarthritis patients, JCI Insight 4 (2) (2019).
[52] T.L. Fernandes, A.H. Gomoll, C. Lattermann, A.J. Hernandez, D.F. Bueno, M. T. Amano, Macrophage: A potential target on cartilage regeneration, Front. Immunol. 11 (2020) 111.
[53] M. Fan, L. Qiang, Y. Wang, Y. Liu, H. Zhuang, R. Guo, Y. Ben, Q. Li, P. Zheng, 3D bioprinted hydrogel/polymer scaffold with factor delivery and mechanical support for growth plate injury repair, Front. Bioeng. Biotechnol. 11 (2023).
[54] W.S. Toh, R.C. Lai, J.H.P. Hui, S.K. Lim, MSC exosome as a cell-free MSC therapy for cartilage regeneration: Implications for osteoarthritis treatment, Semin. Cell Dev. Biol. 67 (2017) 56–64.
[55] S.C. Tao, T. Yuan, Y.L. Zhang, W.J. Yin, S.C. Guo, C.Q. Zhang, Exosomes derived from miR-140-5p-overexpressing human synovial mesenchymal stem cells enhance cartilage tissue regeneration and prevent osteoarthritis of the knee in a rat model, Theranostics 7 (1) (2017) 180–195.
[56] G. Mao, Z. Zhang, S. Hu, Z. Zhang, Z. Chang, Z. Huang, W. Liao, Y. Kang, Exosomes derived from miR-92a-3p-overexpressing human mesenchymal stem cells enhance chondrogenesis and suppress cartilage degradation via targeting WNT5A, Stem Cell Res. Ther. 9 (1) (2018) 247.
[57] H. Guo, F. Li, H. Qiu, W. Xu, P. Li, Y. Hou, J. Ding, X. Chen, Synergistically Enhanced Mucoadhesive and Penetrable Polypeptide Nanogel for Efficient Drug Delivery to Orthotopic Bladder Cancer, Research (Washington, D.C.) 2020 (2020) 8970135.
[58] J. Melrose, C. Shu, J.M. Whitelock, M.S. Lord, The cartilage extracellular matrix as a transient developmental scaffold for growth plate maturation, Matrix Biol. 52–54 (2016) 363–383.
[59] F.H. Zhou, B.K. Foster, G. Sander, C.J. Xian, Expression of proinflammatory cytokines and growth factors at the injured growth plate cartilage in young rats, Bone 35 (6) (2004) 1307–1315.
[60] S.A. Hallett, W. Ono, N. Ono, Growth Plate Chondrocytes: Skeletal Development, Growth and Beyond, International journal of molecular sciences, 2019.
[61] W.E. Samsa, X. Zhou, G. Zhou, Signaling pathways regulating cartilage growth plate formation and activity, Semin. Cell Dev. Biol. 62 (2017) 3–15.
[62] M. Hou, B. Tian, B. Bai, Z. Ci, Y. Liu, Y. Zhang, G. Zhou, Y. Cao, Dominant role of in situ native cartilage niche for determining the cartilage type regenerated by BMSCs, Bioact. Mater. 13 (2022) 149–160.